NASA

Flight-Determined Subsonic Longitudinal Stability and Control Derivatives of the F-18 High Angle of Attack Research Vehicle (HARV) With Thrust Vectoring

Kenneth W. Iliff
Dryden Flight Research Center
Edwards, California

Kon-Sheng Charles Wang
SPARTA, Incorporated
Lancaster, California

December 1997

The NASA STI Program Office . . . in Profile

Since its founding, NASA has been dedicated to the advancement of aeronautics and space science. The NASA Scientific and Technical Information (STI) Program Office plays a key part in helping NASA maintain this important role.

The NASA STI Program Office is operated by Langley Research Center, the lead center for NASA's scientific and technical information. The NASA STI Program Office provides access to the NASA STI Database, the largest collection of aeronautical and space science STI in the world. The Program Office is also NASA's institutional mechanism for disseminating the results of its research and development activities. These results are published by NASA in the NASA STI Report Series, which includes the following report types:
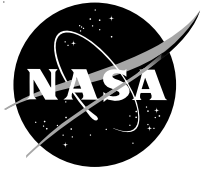
- TECHNICAL PUBLICATION. Reports of completed research or a major significant phase of research that present the results of NASA programs and include extensive data or theoretical analysis. Includes compilations of significant scientific and technical data and information deemed to be of continuing reference value. NASA's counterpart of peer-reviewed formal professional papers but has less stringent limitations on manuscript length and extent of graphic presentations.

- TECHNICAL MEMORANDUM. Scientific and technical findings that are preliminary or of specialized interest, e.g., quick release reports, working papers, and bibliographies that contain minimal annotation. Does not contain extensive analysis.

- CONTRACTOR REPORT. Scientific and technical findings by NASA-sponsored contractors and grantees.

- CONFERENCE PUBLICATION. Collected papers from scientific and technical conferences, symposia, seminars, or other meetings sponsored or cosponsored by NASA.

- SPECIAL PUBLICATION. Scientific, technical, or historical information from NASA programs, projects, and mission, often concerned with subjects having substantial public interest.

- TECHNICAL TRANSLATION. English-language translations of foreign scientific and technical material pertinent to NASA's mission.

Specialized services that complement the STI Program Office's diverse offerings include creating custom thesauri, building customized databases, organizing and publishing research results . . . even providing videos.

For more information about the NASA STI Program Office, see the following:

- Access the NASA STI Program Home Page at ***http://www.sti.nasa.gov***

- E-mail your question via the Internet to help@sti.nasa.gov

- Fax your question to the NASA Access Help Desk at (301) 621-0134

- Telephone the NASA Access Help Desk at (301) 621-0390

- Write to:
  NASA Access Help Desk
  NASA Center for AeroSpace Information
  800 Elkridge Landing Road
  Linthicum Heights, MD 21090-2934

Flight-Determined Subsonic Longitudinal Stability and Control Derivatives of the F-18 High Angle of Attack Research Vehicle (HARV) With Thrust Vectoring

Kenneth W. Iliff
Dryden Flight Research Center
Edwards, California

Kon-Sheng Charles Wang
SPARTA, Incorporated
Lancaster, California

CONTENTS

TABLES

FIGURES

ABSTRACT

The subsonic longitudinal stability and control derivatives of the F-18 High Angle of Attack Research Vehicle (HARV) are extracted from dynamic flight data using a maximum likelihood parameter identification technique. The technique uses the linearized aircraft equations of motion in their continuous/discrete form and accounts for state and measurement noise as well as thrust-vectoring effects. State noise is used to model the uncommanded forcing function caused by unsteady aerodynamics over the aircraft, particularly at high angles of attack. Thrust vectoring was implemented using electrohydraulically-actuated nozzle postexit vanes and a specialized research flight control system. During maneuvers, a control system feature provided independent aerodynamic control surface inputs and independent thrust-vectoring vane inputs, thereby eliminating correlations between the aircraft states and controls. Substantial variations in control excitation and dynamic response were exhibited for maneuvers conducted at different angles of attack. Opposing vane interactions caused most thrust-vectoring inputs to experience some exhaust plume interference and thus reduced effectiveness. The estimated stability and control derivatives are plotted, and a discussion relates them to predicted values and maneuver quality.

NOMENCLATURE

Acronyms

ANSER	Actuated Nose Strakes For Enhanced Rolling
AOA	angle of attack, deg
CFD	computational fluid dynamics
CG	center of gravity
DPRAM	dual-port random access memory
EEPROM	electrically erasable programmable read-only memory
FCC	flight control computer
FCS	flight control system
HARV	High Angle of Attack Research Vehicle
HATP	High Angle of Attack Technology Program
LEF	leading-edge flap (also used as subscript)
LEX	leading-edge extension
MAC	mean aerodynamic chord, ft
MC	mission computer
OBES	onboard excitation system
PCM	pulse code modulation
PID	parameter identification
RAM	random access memory

RFCS	research flight control system
SSI	single-surface input
TEF	trailing-edge flap (also used as subscript)
TVCS	thrust-vectoring control system
UART	universal asynchronous receiver-transmitter

Symbols

a_N	normal acceleration, g
$\mathbf{A}$, $\mathbf{B}$, $\mathbf{C}$, $\mathbf{D}$, $\mathbf{F}$, $\mathbf{G}$	system matrices
b	reference span, ft
c	reference chord, ft
C_A	coefficient of axial force
C_l	coefficient of rolling moment
C_m	coefficient of pitching moment
$C_{m_{bias}}$	coefficient of pitching moment due to bias
C_{m_q}	coefficient of pitching moment due to pitch rate, rad^{-1}
C_{m_α}	coefficient of pitching moment due to angle of attack, deg^{-1}
$C_{m_{\delta_e}}$	coefficient of pitching moment due to stabilator (elevator) deflection, deg^{-1}
$C_{m_{\delta_{pv}}}$	coefficient of pitching moment due to pitch vane input, ft/deg
$C_{m_{\delta_{sa}}}$	coefficient of pitching moment due to symmetric aileron deflection, deg^{-1}
$C_{m_{\delta_{TEF}}}$	coefficient of pitching moment due to trailing-edge flap deflection, deg^{-1}
C_n	coefficient of yawing moment
C_N	coefficient of normal force
$C_{N_{bias}}$	coefficient of normal force due to bias
C_{N_q}	coefficient of normal force due to pitch rate, rad^{-1}
C_{N_α}	coefficient of normal force due to angle of attack, deg^{-1}
$C_{N_{\delta_e}}$	coefficient of normal force due to stabilator (elevator) deflection, deg^{-1}
$C_{N_{\delta_{pv}}}$	coefficient of normal force due to pitch vane input, deg^{-1}

$C_{N_{\delta_{sa}}}$	coefficient of normal force due to symmetric aileron deflection, deg^{-1}
$C_{N_{\delta_{TEF}}}$	coefficient of normal force due to trailing-edge flap deflection, deg^{-1}
C_Y	coefficient of lateral force
$f_{\dot{\alpha}}$	state noise gain for $\dot{\alpha}$
$f_{\dot{q}}$	state noise gain for $\dot{q}$
f	system state function
g	system observation function
g	gravitational force, 32.2 ft/sec^2
$\mathbf{GG^*}$	measurement noise covariance matrix
$\mathbf{H}$	approximation to the information matrix
i	general index
I_x	moment of inertia about roll axis, slug-ft^2
I_{xy}, I_{xz}, I_{yz}	cross products of inertia, slug-ft^2
I_y	moment of inertia about pitch axis, slug-ft^2
I_z	moment of inertia about yaw axis, slug-ft^2
J	cost function
L	iteration number
L_1	normalized load on left engine upper vane
L_2	normalized load on left engine outer vane
L_3	normalized load on left engine inner vane
m	aircraft mass, slug
M	pitching moment, ft-lb
N	normal force, lb
N	number of time points
$\mathbf{n}$	state noise vector
$n_{\dot{\alpha}}$	state noise vector for $\dot{\alpha}$
$n_{\dot{q}}$	state noise vector for $\dot{q}$
p	roll rate, deg/sec

$\dot{p}$	roll acceleration, deg/sec^2
q	pitch rate, deg/sec
$\dot{q}$	pitch acceleration, deg/sec^2
$\bar{q}$	dynamic pressure, lb/ft^2
r	yaw rate, deg/sec
$\dot{r}$	yaw acceleration, deg/sec^2
$\mathbf{R}$	innovation covariance matrix
s	reference area, ft^2
t	time, sec
T	thrust, lb
T_R	computed right-engine thrust, lb
T_L	computed left-engine thrust, lb
$\mathbf{u}$	known control input vector
V	aircraft velocity, ft/sec
V_1	left engine upper vane position, deg
V_2	left engine outer vane position, deg
V_3	left engine inner vane position, deg
V_4	right engine upper vane position, deg
V_5	right engine outer vane position, deg
V_6	right engine inner vane position, deg
$\mathbf{x}$	state vector
$\dot{\mathbf{x}}$	time derivative of state vector
$\tilde{\mathbf{x}}_\xi$	predicted state estimate
$\mathbf{z}$	observation vector
$\tilde{\mathbf{z}}_\xi$	predicted Kalman filter estimate
α	angle of attack, deg
$\dot{\alpha}$	rate of change for angle of attack, deg/sec
β	angle of sideslip, deg

4

$\dot{\beta}$	rate of change for angle of sideslip, deg/sec
δ_e	elevator (symmetric stabilator) deflection, deg
δ_{pv}	equivalent pitch vane input (deflection $\times$ thrust), deg-lb
δ_{sa}	symmetric aileron deflection, deg
δ_{TEF}	trailing-edge flap deflection, deg
δ_{yv}	equivalent yaw vane input (deflection $\times$ thrust), deg-lb
η	measurement noise vector
θ	pitch attitude, deg
$\dot{\theta}$	rate of change of pitch attitude, deg/sec
ξ	unknown parameter vector
$\hat{\xi}$	estimate of ξ
∇_ξ	gradient with respect to ξ
ϕ	roll attitude, deg
$\dot{\phi}$	rate of change for roll attitude, deg/sec
$\dot{\psi}$	rate of change for heading attitude, deg/sec

Superscript

*	transpose of a vector or matrix

INTRODUCTION

During the past decade, significant progress has been made in high-angle-of-attack (high-AOA) research and technology for high-performance military aircraft. Motivated by the tactical advantage of enhanced high-AOA agility and poststall maneuverability, aircraft designers and researchers from industry and government have moved beyond simply studying stall and spin characteristics to actually exploring the poststall region of the high-AOA flight envelope.

Previously, the potential for stall resulting from separated flow over large regions of lifting surfaces prevented pilots from venturing past aircraft AOA limits for any appreciable length of time. In recent years, however, a series of unique fighter-class aircraft has opened up the high-AOA regime as a safe and viable portion of the flight envelope. These aircraft include the innovative, forward-swept wing X-29A and a trio of thrust-vectoring aircraft: the Enhanced Fighter Maneuverability X-31, the Multi-Axis Thrust Vectoring F-16, and the NASA F-18 High Angle of Attack Research Vehicle (HARV). Designs implemented in the F-22 Advanced Tactical Fighter and in prototypes of the Joint Strike Fighter underscore the

value and utility of thrust vectoring. This paper focuses on high-AOA research and parameter identification (PID) to determine the subsonic longitudinal stability and control characteristics of the thrust-vectoring F-18 HARV.

Between 1987 and 1996, research flight testing of the F-18 HARV was conducted at NASA Dryden Flight Research Center, Edwards, California. Modifications to the HARV incorporated a relatively basic thrust-vectoring system, which consisted of three externally-mounted postexit vanes around each of the two engine nozzles along with a specialized flight control system. The design was intended for research purposes only and not for production or operational deployment. The HARV made 388 flights, exploring many unique and important research areas associated with high-AOA flight (as discussed in the next section).

A continuing objective of the flight program was to study the stability and control characteristics of the HARV during thrust-vectoring flight, particularly in the low-speed, high-AOA regime. This paper presents flight-determined subsonic longitudinal stability and control derivatives of the thrust-vectoring HARV extracted from dynamic flight data between 10° and 60° AOA. The 25 flight maneuvers, designed to allow single-surface inputs (SSIs) of aerodynamic controls and independent thrust-vectoring controls, were performed between 1992 and 1994 during flights 156, 226, 250, and 253. The derivatives were extracted with a NASA Dryden-developed PID technique using a maximum likelihood estimator accounting for both state and measurement noise in the linearized aircraft equations of motion. Aerodynamic coefficients in the equations of motion were modified to account for the effects of thrust vectoring. The resulting derivative estimates are plotted as functions of AOA and discussed relative to flight maneuver quality and ground-test and wind-tunnel predictions.

FLIGHT PROGRAM OVERVIEW

In the mid-1980s, NASA embarked on a multiyear program to understand and explore aircraft flight at high AOA (refs. 1–3). NASA Langley Research Center managed the program, known as the High Angle of Attack Technology Program (HATP), with close NASA intercenter involvement from Ames Research Center, Dryden Flight Research Center, and Lewis Research Center. NASA also established active partnerships with industry and academia. In addition, the U.S. Navy, U.S. Air Force, U.S. Marine Corps, and some NATO agencies participated in the HATP. Between 1990 and 1996, NASA hosted biannual conferences dedicated to high-AOA research and technology (refs. 4–6).

The two prime objectives of the HATP were (1) to provide a flight-validated aircraft design methodology through experimental and computational methods that simulate and predict high-AOA aerodynamics, flight dynamics, and flying qualities; and (2) to improve aircraft agility at high AOA while expanding the usable high-AOA envelope. The development of these capabilities involved a close integration of ground-based and flight activity, including wind-tunnel tests (refs. 7–10), computational fluid dynamics (CFD) modeling (refs. 11–15), piloted simulations, advanced flight controls (refs. 16–20), and flight tests to focus on high-AOA aerodynamics, advanced high-AOA control concepts, and maneuver management. Access to full-scale flight conditions was deemed essential to address inherent shortcomings of subscale model and ground tests. In addition, flight validation was expected to provide a more accurate evaluation of the emerging technologies, methods, and concepts being used.

The aircraft selected for the flight portion of the HATP was a McDonnell Douglas F/A-18, subsequently named the F-18 HARV (fig. 1). Previously used for high-AOA and spin research testing at the

Naval Air Test Center, Patuxent River, Maryland, the aircraft was last flown by the Navy in September 1982. Two years later, in October 1984, the aircraft was transferred to NASA and was trucked to NASA Dryden. In the fall of 1985, major efforts to reassemble the aircraft began, along with removing any unnecessary flight test wiring and installing a new research data system. On April 2, 1987, first flight was performed at NASA Dryden, and on May 15, 1996, after 388 flights, testing ended according to the three-phase program schedule of the HATP. Reference 21 provided a more detailed overview of the HARV flight program and an accompanying reference list.

Phase I began in April 1987 and continued through 1989; in this period the F-18 HARV flew 101 research missions, investigating high-AOA aerodynamics and handling characteristics up to 55° AOA. Phase I also examined developmental issues of the HARV research instrumentation suite and established initial aerodynamic correlations between predictions and in-flight measurements (refs. 22–26). Receiving particular attention were the burst location of strong vortices formed off the wing-body-strake (leading-edge extension (LEX)) at high AOA and their role in inducing tail buffet (refs. 27–31). PID was also performed on the basic F-18 HARV during this phase to initially assess stability and control derivatives obtained from wind-tunnel tests and early flight tests by the manufacturer and U.S. Navy (refs. 32–34).

Phase II involved major hardware and software modifications to the HARV, incorporating a multiaxis thrust-vectoring control system (TVCS) and research flight control system (RFCS), both described in greater detail in the next section. This phase, from mid-1991 to late-1994, aggressively expanded the HARV flight envelope. Demonstrated capabilities include stabilized flight at 70° AOA and rolling at high rates at 65° angle of attack.

Phase III flight activities, began in 1995 and completed by May 1996, investigated advanced aerodynamic control concepts. These tests focused on the implementation of actuated forebody strakes mounted conformally on the nose of the HARV to enhance directional control at high AOA (refs. 35 and 36). This paper addresses the analysis and results of PID based on 25 subsonic longitudinal stability and control maneuvers performed during 4 phase II flights involving thrust vectoring.

VEHICLE DESCRIPTION

Many details about the vehicle described in this section are from references 17, 37, 38, and 39; for a more complete treatment of this and related topics, please refer to these documents. The following sections describe the hardware configuration, TVCS, software configuration, control laws, and thrust-vectoring mixer for the HARV.

Hardware Configuration

The aircraft testbed was the sixth full-scale developmental F-18, a single-place, twin-engine, fighter-attack aircraft built for the U.S. Navy by McDonnell Douglas Corporation (St. Louis, Missouri) and Northrop-Grumman Corporation (Los Angeles, California). The Navy previously used this particular aircraft (serial number 160780) for high-AOA and spin testing. The F-18 HARV is powered by two General Electric (Lynn, Massachusetts) F404-GE-400 afterburning engines, rated at approximately 16,000 lb static thrust at sea level. The aircraft features a midwing configuration with a wing-body strake or wing-root LEX that extends from the forward portion of the fuselage and blends into the wing. The configuration under study, dating from 1992 to 1994, carried the LEX fence modification introduced in early 1989

to reduce vertical tail buffet caused by impingement of the LEX vortex; this configuration did not include the actuated forebody strakes used during phase III. As flown, the HARV carried no external stores and was highly instrumented for research purposes. The wingtip launching rails and missiles were replaced with specially designed airdata sensors and camera pods (as fully described in the "Instrumentation and Data Acquisition" section). The in-flight refueling capability and tail-arresting hook were retained. Figure 2 shows a three-view drawing of the HARV, along with major physical characteristics.

The F-18 HARV has five pairs of conventional aerodynamic control surfaces: stabilators, rudders, ailerons, leading-edge flaps (LEFs), and trailing-edge flaps (TEFs). The twin vertical stabilizers, with trailing-edge rudders, are canted outboard approximately 20° from the vertical. The collective deflection of the all-movable horizontal stabilators (δ_e), symmetric LEFs, and symmetric TEFs (δ_{TEF}) provides conventional pitch control. For the longitudinal PID maneuvers addressed here, symmetric ailerons (δ_{sa}) were also evaluated for control in the pitch axis. Roll control uses the ailerons, differential stabilator, and asymmetric LEFs and TEFs. Symmetric rudder deflection and a rudder-to-aileron interconnect (RAI) provide directional control. In addition, the FCS augments lateral-directional control with an aileron-to-rudder interconnect (ARI). Symmetric aileron droop and rudder toe-in are employed in the power approach configuration. A speed brake is on the upper aft fuselage, between the vertical stabilizers. Table 1, reproduced from reference 37, lists maximum control surface position and rate limits.

Table 1. F-18 aerodynamic control surface position and rate limits.

Surface	Position limit, deg	Rate limit, deg/sec
Stabilator:		
Trailing-edge up	24	40
Trailing-edge down	10.5	40
Aileron:		
Trailing-edge up	24	100
Trailing-edge down	45	100
Rudder:		
Trailing-edge left	30	82
Trailing-edge right	30	82
Trailing-edge flap:		
Up	8	18
Down	45	18
Leading-edge flap:		
Up	3	15
Down	33	15
Speed brake:		
Trailing-edge up	60	20–30

Thrust-Vectoring Control System

The addition of a TVCS required significant hardware and software modifications to the aircraft. As shown in figure 3, externally-mounted nozzle postexit vanes for the vectoring of thrust were added to provide additional pitching and yawing moments. The engines were modified to accommodate the thrust-vectoring vane installation by removing the divergent flap portion of the engine nozzle. Controlled deflection of the vanes (three for each engine), which move into the engine exhaust plume, provides thrust-vectoring capability. The location and geometry of the thrust vanes resulted from tradeoffs between thrust-vectoring performance and possible interference with aerodynamic surfaces and the vanes themselves, as figure 4 shows. The larger top vanes generate a greater nose-down pitching moment, while the inboard and outboard vanes used together generate sufficient nose-up pitching moment. The upper vanes work in conjunction with either outboard or inboard vane to produce yawing moment. Details on the thrust vane mixer controller, which coordinates the combined motions of both aerodynamic and thrust-vectoring controls, will be provided in a later section. Vane actuation is accomplished using modified aileron electrohydraulic actuators. Table 2 shows vane system specifications from reference 37.

Table 2. TVCS specifications on the F-18 HARV.

Vane size, in.	
Upper	20×20
Inner and outer	20×15
Vane area, in^2 (ft^2)	
Upper	358.76 (2.49)
Inner and outer	263.64 (1.83)
Vane position limit, deg	–10 to +25
Vane rate limit, deg/sec	80
Total weight, lb	2,200

To provide clearance for the outer vane actuator housing, the inside trailing edges of the stabilators were modified slightly. The area of a single unmodified stabilator is 44.13 ft^2, and the area removed was 0.89 ft^2. This minor area reduction did not significantly reduce stabilator effectiveness. An emergency spin recovery parachute was installed on the upper aft portion of the fuselage between the two engines. The HARV also has an emergency hydraulic and electrical system in case of inadvertent loss of engine power. Engine control was modified to provide a pilot-selectable turbine discharge temperature bias control for additional engine stall margin at high angles of attack.

Table 3, from reference 21, compares the unmodified and modified F-18 HARV. The total weight difference of 4,119 lb includes approximately 2,200 lb for the TVCS itself; 1,500 lb for the spin chute, emergency systems, and ballast (located in the nosecone for pitch balance); and 419 lb for equipment and wiring not directly associated with the TVCS. The final TVCS design does not represent a production prototype but is strictly an experimental installation for research evaluation of the thrust-vectoring control concept.

Table 3. Comparison of unmodified and modified F-18 HARV.

Parameter	Unmodified[*] (phase I)	Modified[*] (phases II and III)
Weight, lb	31,980	36,099
Reference wing area, ft^2	400	400
Reference mean aerodynamic chord (MAC), ft	11.52	11.52
Reference span, ft	37.4	37.4
Center of gravity		
Percentage of MAC	21.9	23.8
Fuselage reference station	454.33	456.88
Waterline	105.24	105.35
Roll inertia, slug-ft^2	22,040	22,789
Pitch inertia, slug-ft^2	124,554	176,809
Yaw inertia, slug-ft^2	139,382	191,744
Product of inertia, slug-ft^2	–2,039	–2,305
Overall length, ft	56	56
Wing aspect ratio	3.5	3.5
Stabilator span, ft	21.6	21.6
Stabilator area, ft^2	88.26	86.48

[*] In each case, the fuel weight is 6,480 lb, which approximately represents a 60-percent fuel condition. The landing gear is up; clean configuration with pilot and support equipment.

Software Configuration

The TVCS hardware modifications required corresponding software modifications to the flight control system (FCS) and mission computer (MC) (refs. 17 and 38). The FCS for the basic F-18 consists of quadruplex-redundant GE-701E flight control computers (FCCs) running the standard F/A-18 V10.1 flight control law, which is a digitally mechanized fly-by-wire control augmentation system. The basic FCS was modified for HARV by adding an analog interface to the thrust-vectoring vane actuators and a RFCS programmed in Ada (ref. 39).

Figure 5(a), taken from reference 39, shows the F-18 HARV computer architecture. The analog input card and RFCS were installed in spare card slots in the basic GE-701E FCC. The FCC maintains overall and primary control of the aircraft, controls input/output processing functions, communicates with the MC for outer loop control, and displays information through a military standard (MIL-STD-1553) data bus.

The RFCS was added to provide a flexible platform for control law research. The RFCS central processing unit is a Pace (Performance Semiconductor Corp., Sunnyvale, California) MIL-STD-1750A architecture processor slaved to the primary GE-701E computer. With the RFCS engaged, the 701E computer selects the RFCS actuator commands computed by the 1750A computer rather than by the HARV V10.1 control law. Dual-port random access memory (DPRAM) provides the communication link between the 701E and 1750A computers, as illustrated in figure 5(a). The RFCS contains 32,000 words of electrically erasable programmable read-only memory (EEPROM), 16,000 words of ultraviolet

programmable read-only memory (UVPROM), 2,000 words of random-access memory (RAM), and 2,000 words of DPRAM. All RFCS command inputs, feedback inputs, monitor data, and actuator command outputs are communicated to the FCC via the DPRAM, such that the RFCS can be considered an embedded control system.

The aircraft is under RFCS control only during the up-and-away research phases of a HARV flight. First, the RFCS is armed by a cockpit toggle switch. Then, it is engaged (or activated) by the existing nose-wheel steering switch on the control stick. The RFCS is manually disengaged via the arm switch or a paddle switch on the control stick. Autodisengagement may occur if predefined limits on rates, accelerations, engine sensors, or airdata sensors are exceeded. The 701E FCC retains complete failure detection and fault management as well as appropriate mode switching in the event of certain failures. The basic F-18 V10.1 control laws and RFCS control laws run independently, in parallel, and are computed continuously throughout the flight envelope. The backup nature of this architecture allows the RFCS software to be classified as non-safety-of-flight. The basic control laws are used during normal flight with the RFCS disengaged, including takeoff and landing.

A useful and important research tool, called the onboard excitation system (OBES), was also incorporated in the RFCS. Software in the OBES held preprogrammed research and envelope expansion maneuvers, which were used for flutter envelope clearance, control power research, and aerodynamic and control law PID. For aerodynamic PID, the OBES, when activated by the pilot, would command SSIs via the RFCS to select control surfaces. By permitting single-surface aerodynamic control deflections, control surface correlation problems were eliminated from the PID analysis. Typically, the feedback and control augmentation systems of modern fighter aircraft introduce relatively high correlations (near linear dependency) between the aircraft controls and states, complicating the identification of individual control surface effectiveness (ref. 40). Independent thrust-vectoring vane deflections were also available with the OBES; these were not single-vane deflections but rather single-axis deflections, using all vanes to excite responses in either the pitch axis or yaw axis.

Control Laws

The RFCS control laws were originally developed by McDonnell Aircraft Company (St. Louis, Missouri) with the goal of demonstrating the research utility of the TVCS and to allow flight envelope expansion of the RFCS software (ref. 17). The control laws were designed to provide stabilized flight at high AOA as well as large amplitude maneuvering capability at high AOA. This capability was achieved through the integration of both aerodynamic and propulsive controls. Initial design emphasis was placed on the stabilized flight task. The RFCS control laws were designed with a modular approach and implemented in Ada. The RFCS software can be separated into longitudinal, lateral-directional, thrust vane mixer, and gross thrust estimation modules, with the latter two modules discussed in the following section.

The longitudinal control law is an AOA command system that uses pilot stick position, AOA, pitch rate (q), and inertial coupling feedback (via the product of angular rates p and r) as inputs. Inertial coupling feedbacks are used to counteract undesirable cross-axis motion generated at high angular rates. Both stabilator and pitch thrust vectoring are used for rapid commands, but steady-state vectoring is driven to zero (washed out) if collective stabilator is not saturated. This scheme helps to minimize thrust loss caused by vectoring, and reduces thermal loads on the vanes. Trimmed flight above approximately 55° AOA requires a nonzero steady-state pitch thrust vectoring because of stabilator saturation. The control stick is geared to provide an AOA of 70° at 5 in. of aft stick deflection. The control system selects

airdata-measured AOA below 25° AOA and selects INS-computed AOA above 30° AOA. The control system fades between the two angles from 25°and 30° AOA.

The lateral-directional control laws use stability axis roll and yaw rate, lateral acceleration, sideslip rate, and inertial coupling (product of p and q, directional only) as feedback signals. Differential stabilator, aileron, differential TEFs, rudder, and yaw vectoring are used for stabilization, coordination, and maneuvering flight. Differential LEFs are not used. Differential stabilator command is limited as a function of AOA and symmetric stabilator command to maintain pitch command priority. The lateral-directional control law provides a feet-on-the-floor stability axis roll rate command capability; lateral stick commands stability axis roll rate apart from rudder pedal inputs that command sideslip angle. At low AOA and higher Mach numbers, the RFCS uses lateral-directional commands from the basic F-18 control laws with the addition of some yaw thrust vectoring to augment rudder power.

As new software versions of the RFCS control law integrating the thrust-vectoring system became available, configuration control of the various versions was necessary. The original control law was provided by McDonnell Aircraft Company, as described earlier, and close revisions to it included RFCS version sets 22, 24, 26, and 28. These early versions, used during most of phase II and all the flights studied in this paper, were referred to as the NASA-0 RFCS control law. During the end of phase II, NASA Langley, with help from NASA Dryden, developed a control law called NASA-1A, which first flew successfully on flight 256 on June 3, 1994. Control law NASA-1A used a technique called variable-output feedback gain to design the longitudinal axis. An eigenstructure-assignment design procedure, known as control power, robustness, agility, and flying qualities tradeoffs, was used in the lateral-directional axes in combination with a control power allocation technique called pseudocontrols. During phase III, the addition of nose-mounted conformal strakes (actuated nose strakes for enhanced rolling (ANSER)) required a new ANSER control law to complement the NASA-1A thrust-vectoring control law. Reference 21 provided additional discussion of and references for these control system features.

When the RFCS is armed, the basic F-18 control system sets the turning vanes to a predetermined ready position (the 0° vane deflection position). The V10.1 control laws continue to control the aircraft until the pilot engages the RFCS, at which point the turning vanes move to the edge of the exhaust plume boundary (approximately 8°–10° vane deflection depending on nozzle pressure ratio) as the RFCS control laws take over. The integrated coordination of the six thrust-vectoring vanes is performed by a RFCS function known as the mixer.

Thrust-Vectoring Mixer

To interface the flight control laws with the thrust-vectoring vanes, a mixer was developed to translate the pitch and yaw thrust-vectoring commands from the RFCS into appropriate vane commands for distribution to the actuators. Although it is possible to command the six thrust-vectoring vanes individually from within the inner-loop control laws (similar to aerodynamic surfaces), the mixer function was designed to accomplish the complex task of computing the proper thrust-vane deflections required to achieve the desired moments from a separate software module.

The mixer was developed by McDonnell Aircraft Company from the results of high-pressure cold-jet tests conducted at NASA Langley using a 14.25-percent-scale nozzle of the TVCS (refs. 41–44). Because the total moment achieved from thrust vectoring is a function of the vane deflection angle as well as the thrust level, the RFCS calculates pitch and yaw thrust-vectoring commands in terms of

degrees of vectored-thrust deflection on the basis of a reference gross thrust. The mixer then uses the results of a real-time thrust estimation algorithm to scale the RFCS-commanded thrust-vectoring moments to the thrust available and to adjust the vane angles to produce the desired control moments. In this way, the apparent thrust-vectoring effectiveness is independent of engine thrust (within the range of the vane position limits and accuracy of the thrust computation). Gross thrust for each engine is estimated individually from nozzle exit radius, engine pressure ratio, and power lever angle for the left or right engine (ref. 45). The mixer requires nozzle pressure ratio, estimated gross thrust, nozzle exit radius from each engine, and the desired vectoring commands to produce the six thrust vane actuator commands. Position, rate, and load limiting are also accounted for by the mixer. In addition to the NASA Langley 14.25-percent-scale cold jet tests, reference 46 described independent subscale laboratory tests to predict thrust-vectoring effectiveness.

Figure 5(b), taken from reference 17, shows a simplified diagram of the thrust vane mixer function. The original corporate report on the theory and implementation of the mixer is found in reference 47.

Toward the end of phase II of the HARV flight program and after the flights examined here, newer versions of the mixer were studied. The original mixer was subsequently called mixer 1. Only one of the several revisions, however, mixer 4.2, was carried through to flight. Mixer 4.2 was incorporated in the NASA 1A control law, which was first successfully flown during flight 256 on June 3, 1994. The development of mixer 4.2 was motivated because mixer 1 had no roll-vectoring capability (only pitch and yaw), nor did it prioritize pitch and yaw vectoring when a combination of these commands could not be simultaneously achieved. The new mixer was developed with a numerical optimization technique based on thrust-vectoring effectiveness and thrust-loss data from ground tests and considerations of optimal vane placement of inactive vanes. The primary design requirement was to achieve the commanded thrust-vectoring moments with the smallest error practical while incorporating a pitch-yaw-roll priority logic and meeting structural limitations. A complete description of the design methodology and optimization process used to develop the new mixer is in reference 48. Again, all 4 flights and 25 PID maneuvers studied in this paper were flown with mixer 1.

INSTRUMENTATION AND DATA ACQUISITION

The MC controlled the MIL-STD-1553 multiplex (MUX) data bus, which provided a standard interface for all equipment connected to the bus such as monitoring instrumentation and recording systems. The MC also was the interface between the flight control sensors and computers to the pilot's digital display indicators, which display primary flight information as well as system status, caution, and failure annunciation. Selected flight information could also be presented on the pilot's head-up display.

Research instrumentation included three-axis linear accelerometers, attitude and angular-rate gyros, control surface position transducers, and redundant airdata sensors. Angle of attack was available with production airdata sensors mounted on the forward fuselage, but only up to approximately 35° AOA because of sensor position limits. For this reason, AOA—as well as AOA rate, angle of sideslip, and sideslip rate—was computed in the MC using data from the inertial navigation system. In addition to inertially-derived airdata, two high-AOA airdata systems were developed. One system used swiveling (self-aligning) pitot probes with conventional AOA and sideslip vanes mounted on both wingtips (ref. 49). A second system used a pneumatic flush airdata system consisting of several pressure sensors located around the tip of the HARV nosecone (refs. 50–52). Airdata from both systems were used for postflight data analysis. Additionally, airdata from the wingtip swivel probes were used for real-time

cockpit display and control-room monitoring. Airdata used in the present PID analysis were taken from the wingtip probes.

Many other parameters were measured to study high-AOA flight. Additional instrumentation included 75 thermocouples and 14 strain gauges on the thrust-vectoring system for monitoring temperatures and loads. Nearly 400 static pressure orifices were installed on the forebody and LEX to characterize the forebody pressure distribution (refs. 25 and 26). Off-surface flow visualizations of the forebody and LEX vortices were obtained using a smoke-generation system that emits particles at the nosetip and the LEX apex (refs. 27 and 53). Four video cameras and one still camera were used to photograph the flow. Surface flow visualization was examined using conventional tufts as well as an emitted fluid technique (ref. 23). Flow-visualization and pressure data were used to correlate with and validate external flow CFD codes (refs. 11–15) and full-scale wind-tunnel predictions (refs. 7 and 8).

Both engines were instrumented to monitor engine operation and were equipped with a real-time thrust measurement system (ref. 45). The right engine had additional instrumentation for engine and inlet diagnostics, with 63 pressure sensors installed along the inlet lip and down the duct to measure inlet distortion at high AOA. An inlet rake with 40 high-response pressure sensors was also installed just forward of the right-engine compressor face to study compressor stalls during high-AOA dynamic flight (ref. 54). Data from the inlet sensors and inlet rake also validated internal flow CFD analyses of the F-18 HARV inlet (refs. 55 and 56).

Data measurements and video signals were telemetered to ground stations for real-time monitoring in the control room, and were recorded for postflight analysis. The telemetry system comprised two independent, asynchronous, pulse code modulation (PCM) data encoders, each with a basic PCM word size of 10 bits. All outputs of the encoders were sent by telemetry to the ground, as no onboard recording of PCM data was available. Special provisions were incorporated in the data acquisition system for higher resolution signals of certain types of data. As many as 2,000 parameters could be telemetered on the two PCM telemetry streams, with data rates as high as 2,142 Hz on select signals.

Flight data used in the present PID analysis were acquired from ground-recorded data and thinned to a final sample rate of 40 Hz. Measurements of AOA and sideslip were corrected for center-of-gravity (CG) offset. Corrections for upwash, sidewash, and boom-bending effects were also made for boom-obtained airdata. Linear accelerometer data were corrected in the PID program for instrument offsets from the CG. Transducers were also available for measuring engine operation and fuel consumption, from which instantaneous mass and inertia characteristics could be calculated. Furthermore, before the maneuvers were analyzed, the data were corrected for time lags introduced by sensor dynamics and signal filtering. Making these corrections was critical to adequately estimate stability and control derivatives (ref. 40).

METHODS OF ANALYSIS

Parameter Identification Formulation

A primary purpose of the HARV flight program was to evaluate the aircraft configuration during high-AOA flight. While flying at high AOA, significant flow separation and vortical flow over the aircraft causes the vehicle to exhibit uncommanded responses. Reference 57 presented a discussion of maneuver difficulties and related analysis issues under these conditions for the 3/8-scale F-15 Remotely Piloted Vehicle aircraft at AOA from –20° to 53°. At high AOA, the uncommanded motions vary from

relatively small amplitude, high-frequency disturbances to very large wing rocking motions to complete rolloff from the flight condition. In addition to being bothersome to the pilot, the motions also complicate the extraction of stability and control derivatives from the planned stability and control maneuvers (ref. 57). The OBES aided the present analysis by augmenting the RFCS control laws and allowing for SSIs. To better analyze the existing maneuvers, it was necessary to account for the uncommanded portions of the aircraft motion.

The procedure implemented in this analysis used state noise to model the uncommanded forcing function. References 58, 59, and 60 completely described this technique. The technique applied to the HARV data also required that the normal aircraft equations of motion be linear in the aerodynamic coefficients; this presented no particular difficulty because the normal stability and control derivatives were already locally linear approximations of nonlinear aircraft aerodynamics.

To perform the analysis presented in this report, an existing parameter estimation computer program was modified to properly account for the additional complexity required to include the effects of the state noise (inputs due to separated and vortical flows) on the stability and control maneuvers. A brief description of the state noise algorithm follows.

A precise, mathematically probabilistic statement of the parameter estimation problem is possible. The first step is to define the general system model (aircraft equations of motion). This model can be written in the continuous/discrete form as follows:

$$\mathbf{x}(t_0) = \mathbf{x}_0 \tag{1}$$

$$\dot{\mathbf{x}}(t) = f\left[\mathbf{x}(t), \mathbf{u}(t), \xi\right] + \mathbf{F}(\xi)\mathbf{n}(t) \tag{2}$$

$$\mathbf{z}(t_i) = g\left[\mathbf{x}(t_i), \mathbf{u}(t_i), \xi\right] + \mathbf{G}(\xi)\eta_i \tag{3}$$

where $\mathbf{x}$ is the state vector, $\mathbf{z}$ is the observation vector, f and g are system state and observation functions, $\mathbf{u}$ is the known control input vector, ξ is the unknown parameter vector, $\mathbf{n}$ is the state noise vector, η is the measurement noise vector, $\mathbf{F}$ and $\mathbf{G}$ are system matrices, and t is time. The state noise vector is assumed to be zero-mean, white Gaussian, and stationary; and the measurement noise vector is assumed to be a sequence of independent Gaussian random variables with zero mean and identity covariance. For each possible estimate of the unknown parameters, a probability that the aircraft response time histories attain values near the observed values can then be defined. The maximum likelihood estimates are defined as those that maximize this probability. Maximum likelihood estimation has many desirable statistical characteristics; for example, it yields asymptotically unbiased, consistent, and efficient estimates.

If equations (2) and (3) are linearized (as is the case for the stability and control derivatives in the aircraft problem), then

$$\mathbf{x}(t_0) = \mathbf{x}_0 \tag{4}$$

$$\dot{\mathbf{x}}(t) = \mathbf{A}\mathbf{x}(t) + \mathbf{B}\mathbf{u}(t) + \mathbf{F}\mathbf{n}(t) \tag{5}$$

$$\mathbf{z}(t_i) = \mathbf{C}\mathbf{x}(t_i) + \mathbf{D}\mathbf{u}(t_i) + \mathbf{G}\eta_i \tag{6}$$

where **A**, **B**, **C**, and **D** are system matrices.

When state noise is important, the nonlinear form of equations (1) to (3) is intractable. For the linear model defined by equations (4) to (6), the cost function (i.e., a function of the difference between the measured and computed time histories) that accounts for state noise is as follows:

$$J(\xi) = \frac{1}{2} \sum_{i=1}^{N} \left[\mathbf{z}(t_i) - \tilde{\mathbf{z}}_\xi(t_i) \right]^* \mathbf{R}^{-1} \left[\mathbf{z}(t_i) - \tilde{\mathbf{z}}_\xi(t_i) \right] + \frac{1}{2} N \ln|\mathbf{R}| \tag{7}$$

where **R** is the innovation covariance matrix and N is the number of time points. The $\tilde{\mathbf{z}}_\xi(t_i)$ term in equation (7) is the Kalman-filtered estimate of **z**.

To minimize the cost function $J(\xi)$, we can apply the Newton-Raphson algorithm, which chooses successive estimates of the vector of unknown coefficients $\hat{\xi}$. Let L be the iteration number. The $L + 1$ estimate of $\hat{\xi}$ is then obtained from the L estimate as follows:

$$\hat{\xi}_{L+1} = \hat{\xi}_L - \left[\nabla_\xi^2 \ J(\hat{\xi}_L) \right]^{-1} \left[\nabla_\xi^* \ J(\hat{\xi}_L) \right] \tag{8}$$

If **R** is assumed fixed, the first and second gradients are defined as follows:

$$\nabla_\xi J(\xi) = - \sum_{i=1}^{N} \left[\mathbf{z}(t_i) - \tilde{\mathbf{z}}_\xi(t_i) \right]^* (\mathbf{G}\mathbf{G}^*)^{-1} \left[\nabla_\xi \tilde{\mathbf{z}}_\xi(t_i) \right] \tag{9}$$

$$\begin{aligned}
\nabla_\xi^2 \ J(\xi) = \ & \sum_{i=1}^{N} \left[\nabla_\xi \tilde{\mathbf{z}}_\xi(t_i) \right]^* (\mathbf{G}\mathbf{G}^*)^{-1} \left[\nabla_\xi \tilde{\mathbf{z}}_\xi(t_i) \right] \\
& - \sum_{i=1}^{N} \left[\mathbf{z}(t_i) - \tilde{\mathbf{z}}_\xi(t_i) \right]^* (\mathbf{G}\mathbf{G}^*)^{-1} \left[\nabla_\xi^2 \ \tilde{\mathbf{z}}_\xi(t_i) \right]
\end{aligned} \tag{10}$$

where $\mathbf{G}\mathbf{G}^*$ is the measurement noise covariance matrix. The Gauss-Newton approximation to the second gradient is as follows:

$$\nabla_\xi^2 \ J(\xi) \cong \sum_{i=1}^{N} \left[\nabla_\xi \tilde{\mathbf{z}}_\xi(t_i) \right]^* (\mathbf{G}\mathbf{G}^*)^{-1} \left[\nabla_\xi \tilde{\mathbf{z}}_\xi(t_i) \right] \tag{11}$$

The Gauss-Newton approximation, which in past reports by the first author was sometimes referred to as modified Newton-Raphson, is computationally much easier than the Newton-Raphson approximation because the second gradient of the innovation never needs to be calculated.

Figure 6 illustrates the maximum likelihood estimation concept. The measured response is compared with the estimated response, and the difference between these responses is called the response error. The

cost function of equation (7) includes this response error. The minimization algorithm is used to find the coefficient values that minimize the cost function. Each iteration of this algorithm provides a new estimate of the unknown coefficients on the basis of the response error. These new estimates are then used to update values of the coefficients of the mathematical model, providing a new estimated response and, therefore, a new response error. Updating of the mathematical model continues iteratively until a convergence criterion is satisfied (i.e., when the ratio of change in the total cost to the total cost, $\Delta J(\xi)/J(\xi)$, is less than 0.000001). The estimates resulting from this procedure are the maximum likelihood estimates.

The maximum likelihood estimator also provides a measure of the reliability of each estimate based on the information obtained from each dynamic maneuver. This measure of the reliability, analogous to the standard deviation, is called the Cramér-Rao bound (refs. 59 and 61). The Cramér-Rao bound, as computed by current programs, should generally be used as a measure of relative, rather than absolute, accuracy. The bound is obtained from the approximation to the information matrix, $\mathbf{H}$, which is based on equation (11); the actual information matrix is defined when evaluated at the correct values (not the maximum likelihood estimates) of all the coefficients. The bound for each unknown is the square root of the corresponding diagonal element of $\mathbf{H}^{-1}$; that is, for the ith unknown, the Cramér-Rao bound is $\sqrt{(\mathbf{H}^{-1}{}_{i,i})}$.

The stability and control derivatives to be presented in the "Results and Discussion" section were analyzed assuming that state noise was present in all maneuver cases.

Equations of Motion

The linearized aircraft equations of motion used in the PID analysis are derived from the more general system of nine coupled nonlinear differential equations that describe the aircraft motion (refs. 62 and 63). These nonlinear equations assume a rigid vehicle and a flat, nonrotating earth. The time rate of change of mass and inertia is assumed negligible, and fuel-sloshing effects are ignored. No small-angle approximations are used, but the absolute values of β and θ must be less than 90° because of singularities at ±90°. The aircraft velocity must not be zero; no symmetry assumptions are made. Engine-thrust terms are included, assuming the engine alignment and thrust vector are along the x-axis. (Terms accounting for thrust vectoring are included in the expressions for the aerodynamic coefficients, to be described later.) The equations are written in body axes referenced to the CG. All angles are in degrees. The $\dot{V}$ and $\dot{\psi}$ equations are not included. The remaining system of state equations is as follows:

$$
\begin{aligned}
\dot{\alpha} \;=\; & q - \tan\beta(p\cos\alpha + r\sin\alpha) - \left[\bar{q}s/(mV\cos\beta)\right](C_N\cos\alpha - C_A\sin\alpha) \\
& + \left[g/(V\cos\beta)\right]\left\{\cos\theta\cos\phi\cos\alpha + \sin\theta\sin\alpha - \left[T/(mg)\right]\sin\alpha\right\}
\end{aligned}
\tag{12}
$$

$$
\begin{aligned}
\dot{\beta} \;=\; & p\sin\alpha - r\cos\alpha + \cos\beta\left[(\bar{q}s)C_Y/(mV) + (g/V)\cos\theta\sin\phi\right] \\
& + \sin\beta\left\{\left[\bar{q}s(C_N\sin\alpha + C_A\cos\alpha)\right]/(mV) \right. \\
& \left. - (g/V)\left[\cos\theta\cos\phi\sin\alpha - \sin\theta\cos\alpha - (T/(mg))\cos\alpha\right]\right\}
\end{aligned}
\tag{13}
$$

17

$$\dot{p}I_x - \dot{q}I_{xy} - \dot{r}I_{xz} = \bar{q}sbC_l + qr(I_y - I_z) + (q^2 - r^2)I_{yz} + pqI_{xz} - rpI_{xy} \tag{14}$$

$$\dot{q}I_y - \dot{r}I_{yz} - \dot{p}I_{xy} = \bar{q}scC_m + rp(I_z - I_x) + (r^2 - p^2)I_{xz} + qrI_{xy} - pqI_{yz} \tag{15}$$

$$\dot{r}I_z - \dot{p}I_{xz} - \dot{q}I_{yz} = \bar{q}sbC_n + pq(I_x - I_y) + (p^2 - q^2)I_{xy} + prI_{yz} - qrI_{xz} \tag{16}$$

$$\dot{\theta} = q\cos\phi - r\sin\phi \tag{17}$$

$$\dot{\phi} = p + r\cos\phi\tan\theta + q\sin\phi\tan\theta \tag{18}$$

Most aircraft, including the F-18 HARV examined here, are nearly symmetric about the *x-z* plane. This symmetry can be used, along with small-angle approximations, to separate the equations of motion into two largely independent sets describing the longitudinal and lateral-directional motions of the aircraft. Some nonlinear terms are linearized through the use of measured data. References 62 and 64 gave a more comprehensive treatment of the aircraft PID linearization problem.

Symmetry and small perturbation approximations allow the longitudinal equations of motion (eqs. (12), (15), and (17)) to be expressed in a form that contains locally linear approximations in the aerodynamic coefficients as required by equation (5) (repeated here):

$$\dot{\mathbf{x}}(t) = \mathbf{A}\mathbf{x}(t) + \mathbf{B}\mathbf{u}(t) + \mathbf{F}\mathbf{n}(t) \tag{5}$$

The aerodynamic terms of interest in equations (12) and (15) are C_N and C_m, respectively. The coefficients C_N and C_m are expanded as follows:

$$
C_N = C_{N_\alpha}\alpha + C_{N_q}qc/(2V) + C_{N_{\delta_e}}\delta_e + C_{N_{\delta_{TEF}}}\delta_{TEF} + C_{N_{\delta_{sa}}}\delta_{sa} + C_{N_{\delta_{pv}}}\delta_{pv}/(\bar{q}s)
$$
$$
+ C_{N_{bias}} \tag{19}
$$

$$
C_m = C_{m_\alpha}\alpha + C_{m_q}qc/(2V) + C_{m_{\delta_e}}\delta_e + C_{m_{\delta_{TEF}}}\delta_{TEF} + C_{m_{\delta_{sa}}}\delta_{sa} + C_{m_{\delta_{pv}}}\delta_{pv}/(\bar{q}sc)
$$
$$
+ C_{m_{bias}} \tag{20}
$$

The unknown stability and control derivatives to be estimated by PID are C_{N_α}, $C_{N_{\delta_e}}$, $C_{N_{\delta_{TEF}}}$, $C_{N_{\delta_{sa}}}$, $C_{N_{\delta_{pv}}}$, $C_{N_{bias}}$, C_{m_α}, C_{m_q}, $C_{m_{\delta_e}}$, $C_{m_{\delta_{TEF}}}$, $C_{m_{\delta_{sa}}}$, $C_{m_{\delta_{pv}}}$, and $C_{m_{bias}}$. (C_{N_q} is not estimated and is fixed at zero in the analysis in this paper.) $C_{N_{\delta_{pv}}}$ and $C_{m_{\delta_{pv}}}$ are, respectively, the coefficients of normal force and pitching moment due to pitch vane input. These derivatives are related back to equation (5) through the following expressions for system matrices $\mathbf{A}$, $\mathbf{B}$, and $\mathbf{F}$ with corresponding state, control, and noise vectors $\mathbf{x}$, $\mathbf{u}$, and $\mathbf{n}$:

$$\mathbf{A} = \begin{bmatrix} C_{N_\alpha}\left[\bar{q}s/(mV)\right] & 1 & 0 \\[2mm] C_{m_\alpha}(\bar{q}sc/I_y) & C_{m_q}(\bar{q}sc/I_y)\left[c/(2V)\right] & 0 \\[2mm] 0 & 1 & 0 \end{bmatrix} \tag{21}$$

$$\mathbf{B} = \begin{bmatrix} C_{N_{\delta_e}}\left[\bar{q}s/(mV)\right] & C_{N_{\delta_{TEF}}}\left[\bar{q}s/(mV)\right] & C_{N_{\delta_{sa}}}\left[\bar{q}s/(mV)\right] & C_{N_{\delta_{pv}}}\left[1/(mV)\right] & C_{N_{bias}}[\bar{q}s/(mV)] \\[2mm] C_{m_{\delta_e}}(\bar{q}sc/I_y) & C_{m_{\delta_{TEF}}}(\bar{q}sc/I_y) & C_{m_{\delta_{sa}}}(\bar{q}sc/I_y) & C_{m_{\delta_{pv}}}(1/I_y) & C_{m_{bias}}(\bar{q}sc/I_y) \\[2mm] 0 & 0 & 0 & 0 & 0 \end{bmatrix} \tag{22}$$

$$\mathbf{F} = \begin{bmatrix} f_{\dot\alpha} & 0 \\[1mm] 0 & f_{\dot q} \\[1mm] 0 & 0 \end{bmatrix} \tag{23}$$

$$\mathbf{x} = \begin{bmatrix} \alpha & q & \theta \end{bmatrix}^{*} \tag{24}$$

$$\mathbf{u} = \begin{bmatrix} \delta_e & \delta_{TEF} & \delta_{sa} & \delta_{pv} & 1 \end{bmatrix}^{*} \tag{25}$$

$$\mathbf{n} = \begin{bmatrix} n_{\dot\alpha} & n_{\dot q} \end{bmatrix}^{*} \tag{26}$$

The state noise coefficients are $f_{\dot\alpha}$ and $f_{\dot q}$, and the state noise is defined as $n_{\dot\alpha}$ and $n_{\dot q}$.

RESULTS AND DISCUSSION

The 25 stability and control maneuvers examined here were all analyzed with the PID technique described in the previous section. All maneuvers were subsonic and performed as small perturbation maneuvers about the 1-g flight condition near AOAs of 10°, 20°, 30°, 40°, 50°, and 60°. The maneuvers were performed by the OBES while the vehicle was under RFCS control as described in the "Software Configuration" section. All maneuvers were analyzed assuming state noise was present as described earlier, although those maneuvers near 10° AOA did not exhibit significant uncommanded motions caused by unsteady flow phenomena.

Variations in control input excitation and dynamic response were exhibited between maneuvers conducted at different average AOAs. Table 4 summarizes these variations. These variations can be understood by examining four typical stability and control maneuvers near 10°, 20°, 30°, and 40° AOA. This discussion is a prelude to a discussion of the resulting derivative estimates and associated limitations of the PID analysis.

Table 4. Summary of OBES-commanded control input amplitudes.

Maneuver number	Average α, deg	$\Delta\alpha$, deg	$\Delta\delta_e$, deg	$\Delta\delta_{TEF}$, deg	$\Delta\delta_{sa}$, deg	δ_{pv}/T range, deg
1	9.6	6	11	29	29	–5 to +5
2	9.8	7	11	29	29	–4 to +3
3	10.6	6	11	29	29	–5 to +5
4	11.0	6	11	30	29	–3 to +3
5	11.4	8	10	29	26	–4 to +4
6	20.2	7	17	33	50	0 to +10
7	20.8	6	17	34	50	0 to +10
8	23.1	8	17	33	50	–2 to +8
9	29.1	8	16	25	46	–2 to +7
10	29.7	5	19	26	50	0 to +10
11	31.3	5	19	26	50	–5 to +10
12	31.3	6	17	26	50	–2 to +7
13	31.9	6	18	26	50	–2 to +7
14	39.0	4	10	15	29	–4 to +4
15	39.8	7	15	25	45	–2 to +7
16	39.8	6	17	25	50	–5 to +7
17	39.9	4	10	15	29	–4 to +4
18	40.9	6	17	25	49	–6 to +6
19	46.7	6	17	25	50	–4 to +8
20	47.9	5	9	15	29	–3 to +3
21	48.2	7	15	25	45	–2 to +7
22	48.4	7	17	25	50	–3 to +8
23	59.5	9	3	15	29	–10 to –30
24	60.2	3	3	15	29	–10 to –30
25	60.3	10	6	25	46	–5 to +2

Stability and Control Maneuvers

Figure 7 illustrates a typical longitudinal maneuver performed near 10° AOA (maneuver 1 in table 4). Figure 7(a) shows the flight condition of the 24-sec maneuver with AOA varying between 7° and 13°, altitude between 32,000 and 30,300 ft, Mach number between 0.47 and 0.57, and dynamic pressure between 88 and 139 lb/ft^2. Figure 7(b) shows the longitudinal response variables used for PID: AOA (α), pitch rate (q), pitch attitude (θ), and normal acceleration (a_N). Figure 7(c) shows the control inputs used to excite the vehicle response: elevator deflection (δ_e), symmetric trailing-edge flap deflection (δ_{TEF}), symmetric aileron deflection (δ_{sa}), pitch-vane input (δ_{pv}), and yaw-vane input (δ_{yv}). The individual vane deflections (V_1, V_2, V_3, V_4, V_5, and V_6 defined in figure 5(b)) are plotted in figure 7(d) along with the thrust from each engine, T_L and T_R, and the total thrust, T.

As figure 5(b) showed, V_1, V_2, and V_3 are the upper-, outer-, and inner-vane deflections for the left engine; and V_4, V_5, and V_6 are the upper-, outer-, and inner-vane deflections for the right engine. If the vanes are assumed to just touch the exhaust plume (an assumption to be discussed later), the equivalent pitch-vane and yaw-vane inputs in figure 7(c) are defined by the following equations:

$$\delta_{pv} = \left\{ \frac{\left[V_1 - \left(\frac{V_2 + V_3}{2} \right) + V_4 - \left(\frac{V_6 + V_5}{2} \right) \right]}{2} \right\} T \tag{27}$$

$$\delta_{yv} = \left\{ \frac{\left[\frac{(V_2 - V_3)}{2} + \frac{(V_6 - V_5)}{2} \right]}{2} \right\} T \tag{28}$$

where T is the total thrust equal to $T_L + T_R$. In figure 7(d), the individual vanes are plotted as longitudinal effector pairs; that is, where the overplotted vane signals agree, a force and moment will result in the longitudinal axes. Where they do not agree, a force and moment will result in the lateral-directional axes. The degree to which the plotted vane signals of figure 7(d) agree or disagree in producing an adequate longitudinal response is illustrated by examining the δ_{pv} and δ_{yv} equivalent vane inputs in figure 7(c), which are computed from equations (27) and (28).

Figure 7(e) shows the least-squares fit between vane positions V_1, V_2, and V_3, and their respective normalized measured loads, L_1, L_2, and L_3, from the left engine. The vanes on the right engine were not instrumented to measure loads. The information contained in the least-squares fits shown in this figure and its implications will be discussed later.

As were all 25 maneuvers discussed in this report, the maneuver shown in figure 7 was performed by OBES with the aircraft under RFCS control. The aircraft responses given in figure 7(b) resulted from the control input excitation given in figure 7(c). Doublets were commanded by the OBES on each of the four vehicle controls in the following sequential order: δ_{TEF}, δ_{sa}, δ_e, and δ_{pv}. The resulting control inputs to the aircraft are shown in figure 7(c), where the doublets and the subsequent effect of the RFCS feedback can be seen for δ_{TEF}, δ_e, and δ_{pv}. In contrast, the symmetric aileron signal does not contain any motion due to feedback. The four control doublets are all very distinct and independent, which is very desirable for PID analysis.

The primary reason to command individual control doublets is to guarantee independent information from all of the controls as well as all of the states. This independence ensures the identifiability of each control and of each state variable. With a feedback system, the control motions can be defined as a function of the fed-back responses and the other control positions, thereby making the states and control positions almost linearly dependent (ref. 40), which is undesirable for identifiability. The independent doublet on each control ensures that this near-linear dependence does not occur. The SSI approach to PID has been investigated for several other flight research programs, including the recent and similarly thrust-vectoring X-31 (ref. 65).

Further inspection of the plotted signals in figures 7(b) and 7(c) shows high correlation between the response and control signals arising from the feedback control system. This correlation is particularly evident by comparing the pitch rate response signal (q) and the pitch vane input signal (δ_{pv}) in the first 16 sec. Note, however, that the OBES-commanded independent δ_{pv} doublet that occurs after 16 sec is free of any correlation and guarantees acceptable identifiability of δ_{pv}. All five maneuvers near 10° AOA looked very similar to the maneuver shown in figure 7.

Figure 8 is a typical maneuver near 22° AOA (maneuver 8 in table 4). Figure 8(a) shows the flight condition for the 18-sec maneuver for an AOA between 19° and 27°, altitude between 29,300 and 28,300 ft, Mach number between 0.39 and 0.37, and dynamic pressure between 69 and 63 lb/ft^2. Figure 8(b) shows the response variables, figure 8(c) shows the control variables, figure 8(d) shows the individual vane positions, and figure 8(e) shows the least-squares fit between the left-engine vanes and the corresponding loads in an analogous fashion to that shown in figure 7. The same observations about the OBES doublets and the independence of the controls can be made for this maneuver as were made for the previous maneuver.

The main difference between this maneuver and the one near 10° AOA, other than flight condition, is that the amplitudes of elevator doublet and symmetric aileron doublet are both 70 percent greater in the current maneuver than in the previous maneuver. Other differences are that the current maneuver has only the positive portion of the δ_{pv} doublet and it is about twice the amplitude. The second (negative) half of the doublet was so large that it caused a change in AOA of more than 20°, resulting in a peak AOA of more than 40°. This large excursion violated the small-perturbation assumptions used to linearize the equations of motion as was mentioned in the "Equations of Motion" section. Therefore, truncation of the maneuver at 18 sec was necessary. In addition to limiting the amount of δ_{pv} information, this truncation eliminated the useful free-oscillation portion following a doublet where there is little control activity, as occurred in the 10° AOA maneuver shown in figure 7 after 21 sec. Similar truncations were required for all eight maneuvers between 20° and 32° AOA. The other two maneuvers near 20° AOA (table 4) were similar to the maneuver shown in figure 8.

Figure 9 presents a 19-sec maneuver near 30° AOA that varies between 27° and 33° AOA (maneuver 13 in table 4). Figure 9(a) shows the flight condition, figure 9(b) shows the response variables, figure 9(c) shows the control variables, figure 9(d) shows the vane positions, and figure 9(e) shows the least-squares fit of the left-engine vanes and the corresponding loads. As with the previous (22° AOA) maneuver, this maneuver and the other four maneuvers near 30° AOA had to be truncated, leaving only the positive portion of the δ_{pv} doublet. The OBES doublet amplitudes for the four other 30° AOA maneuvers are all very similar to those of this maneuver and those of the previous maneuver (table 4). A distinct feature of the 30° AOA maneuvers is that because the AOA remains greater than 27°, the δ_{TEF} are no longer part of the feedback control system, as manifested by the absence of the oscillatory portion of the δ_{TEF} signal that was present in figures 7 and 8.

Figure 10 illustrates a 25-sec maneuver near 40° AOA that varies between 38° and 42° AOA (maneuver 17 in table 4). Figure 10(a) shows the flight condition, figure 10(b) shows the aircraft responses, figure 10(c) shows the control inputs, figure 10(d) shows the individual vane positions, and figure 10(e) shows the least-squares fit of the left-engine vanes with their corresponding loads in a fashion

similar to that for the previous three figures. Because of separated and unsteady flows at this high AOA, all response variables are noticeably noisier than those for the 10° AOA maneuver. In addition, this maneuver is similar to the 10° AOA maneuver shown in figure 7 in that the δ_{pv} doublet need not be truncated to keep the maneuver within the small-perturbation assumptions. An important observation regarding this maneuver is that the δ_{TEF}, δ_{sa}, and δ_e doublets are half the amplitude of the other maneuvers discussed near 20° and 30° AOA, resulting in smaller variations in the response signals. Two of the five maneuvers near 40° AOA have these lower amplitude doublets. The other three 40° AOA maneuvers, however, have the larger amplitude doublets for δ_{TEF}, δ_{sa}, and δ_e as found in the 20° and 30° AOA maneuvers (table 4). The amplitude of the δ_{pv} doublet is the same as that for the 10° AOA maneuver. The δ_{TEF} still shows that it is no longer part of the feedback control system, as the trimmed AOA remains greater than 27°.

The significant variations in amplitude and character of the OBES doublets illustrated by the previous discussion made the interpretation of the PID analysis somewhat cumbersome. Each maneuver in itself is excellent in that sufficient response is obtained from the substantially independent doublet of each control. The overall interpretation of the 25 maneuvers—stimulated by different control input amplitudes—is difficult. In addition, the natural scatter of estimates in the difficult-to-analyze, high-AOA flight regime further obfuscates the interpretation of the data. By taking the aforementioned maneuver differences into account, however, the reader can reach meaningful conclusions, as will be seen in the next section.

Stability and Control Derivative Results

This section presents and discusses the stability and control derivatives resulting from PID. Each stability and control derivative is plotted as a function of AOA, where the circle symbols are the flight estimates, the vertical lines are the uncertainty levels, the solid line is the fairing of the flight estimates based on the authors' interpretation of the flight estimates, and the dashed line is a fairing of the predicted values taken from cold-jet thrust vectoring tests (ref. 41) and a simulation based primarily on wind-tunnel data (refs. 66 and 67). The aerodynamic wind-tunnel data used to characterize the prediction fairing were for the basic F-18 configuration, without accounting for the external modifications made on the HARV which included the thrust-vectoring apparatus and the LEX fences as discussed in the "Hardware Configuration" section. A secondary dashed fairing (dash-dot-dash) on some of the plots is explained later. The uncertainty levels (ref. 40) shown on the plots are obtained by multiplying the Cramér-Rao bound of each estimate by a factor of 5. The fairing of the estimates is based on the uncertainty levels, the scatter of adjacent estimates around a given AOA, and engineering judgment of the maneuver quality. Theoretically, information on maneuver quality such as the length of the maneuver, amount of response signal noise at the time of the control input, excitation of response variables (α, q, θ, and a_N), and the quality of the fit of the maneuver is contained in the value of the uncertainty level. A large uncertainty level indicates low information content on the derivative estimate for that maneuver, and a small level indicates high information content.

The estimation of stability and control derivatives at high AOA is always difficult because of the uncertainty of the aerodynamic mathematical model and the occurrence of uncommanded responses during the dynamic maneuver. The interpretation of the data is complicated for the F-18 HARV because of variations in the amplitudes of the control doublets between maneuvers as pointed out in the last section. Table 4, which showed these amplitude variations, will be referred to frequently in the following discussion to point out how the stability and control derivative plots are interpreted.

Aerodynamic Control Derivatives

Figure 11(a) shows $C_{m_{\delta_e}}$ as a function of AOA. Good overall agreement is seen between predicted and flight-determined values, with the flight values showing somewhat less effectiveness below 38° AOA and somewhat more effectiveness above 38° AOA. The shaded symbols indicate maneuvers with smaller amplitude δ_e doublets, as observed from table 4. In particular, two of these maneuvers are near 40° AOA and a third near 50° AOA, through which a secondary fairing is drawn. This secondary fairing between 40° and 50° AOA indicates that the elevator is somewhat (perhaps 10 percent) more effective for smaller δ_e deflections than for larger δ_e deflections in this AOA range. Perhaps the same would be true at other AOAs, but no evaluation can be made because the δ_e doublets at 10°, 20°, 30°, and 60° AOA are either all large or all small. Figure 11(b) shows $C_{N_{\delta_e}}$ as a function of AOA. The flight value is consistently lower throughout the AOA range than the prediction value. The shaded symbols indicate maneuvers with smaller amplitude δ_e doublets. Here again, the elevator appears more effective for smaller deflections than for larger deflections in the 40° to 50° AOA range.

Figure 12(a) shows the estimates of pitching moment due to trailing-edge flap deflection, $C_{m_{\delta_{TEF}}}$. The flight values are less effective than predicted throughout the AOA range except near 30° where flight and predicted agree. The shaded symbols indicate maneuvers wherein the amplitude of the δ_{TEF} doublet is small (table 4). Two of these symbols are near 40° AOA and another is near 50°. As shown by the secondary fairing through these symbols, the smaller-amplitude δ_{TEF} maneuvers seem to have less effectiveness (less effect on pitching moment) than the larger-amplitude δ_{TEF} maneuvers. Figure 12(b) shows $C_{N_{\delta_{TEF}}}$ as a function of AOA. The flight values are lower than predicted below 42° AOA. The secondary fairing through the shaded symbols near 40° and 50° AOA suggests somewhat more normal force per degree of δ_{TEF} deflection for small deflections than for large deflections.

Figure 13(a) shows the estimates of pitching moment due to symmetric aileron $C_{m_{\delta_{sa}}}$ as a function of AOA. Excellent agreement is seen between flight-determined and predicted values below 40° AOA with the flight values being somewhat less effective above 40° AOA. The shaded symbols indicate maneuvers with smaller δ_{sa} amplitude doublets (table 4), with no apparent effects seen in the estimates because of this variation in amplitude. Figure 13(b) shows $C_{N_{\delta_{sa}}}$ as a function of AOA. Fairly good agreement is seen between flight-derived and predicted values below 30° AOA. A smaller flight value is indicated between 30° and 50° AOA, and a larger value above 50°.

Thrust-Vectoring Control Derivatives

Figure 14(a) gives the coefficient of pitching moment due to pitch vectoring $C_{m_{\delta_{pv}}}$, and figure 14(b) gives the coefficient of normal force due to pitch vectoring, $C_{N_{\delta_{pv}}}$. The mechanization and software driving the thrust vectoring are described in an earlier section. Details on the prediction of the effectiveness of the thrust vectoring are given in references 41–44. Thrust-vectoring effectiveness is defined in terms of the effective plume deflection, measured from the nominal (nonvectoring) thrust line. When the vane is against or inside the plume, this effectiveness has been predicted in reference 41 to be 0.94 deg/deg or 0.0164 rad/deg, which is the ratio of plume deflection to vane deflection for nozzle pressure ratios of 2. The data in reference 41 also show that a similar value is true for nozzle pressure ratios of 4 and 5. All 25 maneuvers presented here had nozzle pressure ratios between 4 and 5. The pitch vane effectiveness is different from the other traditional stability and control derivatives studied in this report in that the δ_{pv} derivatives are not a function of aircraft velocity or dynamic pressure. Because of this difference, the $C_{m_{\delta_{pv}}}$ and $C_{N_{\delta_{pv}}}$ derivatives are normalized by dividing the moment and force by both the vane deflection and thrust (that is, the pitch vane input as defined in equation (27)). Therefore, the units on $C_{m_{\delta_{pv}}}$ is feet per degree and the units on $C_{N_{\delta_{pv}}}$ is 1/degree. The thrust is calculated for each sample point using the method described in reference 45. Then δ_{pv} is calculated by equation (27) and is used as an input to the equations of motion. The derivatives $C_{m_{\delta_{pv}}}$ and $C_{N_{\delta_{pv}}}$ are then estimated the same way as all the other derivatives, as described earlier in the "Parameter Identification Formulation" section. The predicted value of $C_{N_{\delta_{pv}}}$ is 0.0164 deg^{-1}; and the predicted value of $C_{m_{\delta_{pv}}}$, based on a moment arm of approximately 20 ft between the aircraft CG and the center of the vanes, is –0.328 ft/deg.

Figure 14(a) shows the flight-determined values of $C_{m_{\delta_{pv}}}$ to be about –0.25 ft/deg up to 30° AOA, with gradually decreasing magnitudes at higher AOA. Poor agreement is seen with the prediction of –0.328 ft/deg. The primary reason for this decreased effectiveness is found by examining figures 7(e), 8(e), 9(e), and 10(e). As mentioned earlier, these figures compare individual vane deflection with the least-squares fit of the normalized load on the corresponding thrust-vectoring vane. By inspecting these figures, one can see that the deflection of a single vane affects the load on the opposing vane or vanes. For instance, figure 7(e) shows a δ_{pv} doublet that occurs at 17 to 21 sec. Before the doublet, the individual vanes are positioned by the RFCS to just touch the plume, which turns out to be about a 9° or 10° vane deflection.

When V_1, the left-engine upper vane, is deflected into the plume at 17 sec, a load is seen to increase on V_2, the outer vane, and on V_3, the inner vane, although there is no corresponding deflection of either vanes V_2 or V_3. The same effect can be seen when V_2 and V_3 are deflected into the plume that a load with the same signal shape as deflections V_2 and V_3 appears on the opposing vane V_1. For the approximately 5° deflection of an activated vane during a doublet, a corresponding load amounting to from 1° to 1.5° is observed in the opposing inactive vane. The impingement of the vectored plume on the opposing vane or vanes will result in reduced effectiveness. For the remainder of this discussion, this effect will be called plume pinching. Thus, for the large 5° deflections of the δ_{pv} doublet, the 1° to 1.5° apparent deflection on the opposing vanes would result in a 20- to 30-percent reduction in pitch vane effectiveness. The same effect can be seen for the other three maneuvers at 20°, 30°, and 40° AOA (figs. 8(e), 9(e), and 10(e)). The plume-pinching effect can be seen on all four maneuvers to a lesser extent on smaller δ_{pv} deflections partially caused by the least-squares technique weighting the large deflections the most.

The potential 20- to 30-percent reduction in effectiveness is about that seen in figure 14(a) for $C_{m_{\delta_{pv}}}$ between 10° and 30° AOA. The reduced effectiveness above 30° may be caused by additional effects of the free airstream. The much-reduced effectiveness at 60° AOA may result from the exact point of contact between the vane and the plume being more difficult to identify. Also, because the stabilator is saturated for trimmed flight above 55° AOA (as was discussed in the "Control Laws" section), a nonzero steady-state δ_{pv} is required to maintain 60° AOA flight. Thus, the actual δ_{pv} doublet is commanded in addition to this nonzero pitch vane input. Taking into consideration the previous discussion, the agreement between flight-determined and predicted values of $C_{m_{\delta_{pv}}}$ is very good up to 30° AOA and fairly good at 40° and 50° AOA.

Figure 14(b), the $C_{N_{\delta_{pv}}}$ derivative, shows good agreement between flight-determined and predicted values from 10° to 30° AOA without accounting for plume pinching. Above 30° AOA, the comparison is not as good, as the flight and maneuver conditions are similar to those found for $C_{m_{\delta_{pv}}}$ above 30° AOA. Further analysis showed that $C_{N_{\delta_{pv}}}$ was being defined primarily by the small-amplitude δ_{pv} portions of the maneuver. When the data were reanalyzed using only the doublet portion (5° large-amplitude input) of the maneuver, the $C_{N_{\delta_{pv}}}$ also showed the effects of plume pinching. This pinching effect can be seen in figure 14(c) where the results of the doublet-only portion (shaded symbols) are plotted along with the original results shown in figure 14(b). Figure 14(c) reveals a 20-percent reduction in $C_{N_{\delta_{pv}}}$ due to plume pinching when only the large amplitude portions of the maneuvers are considered at 10° and 20° AOA. This reduction in effectiveness is similar to that seen for $C_{m_{\delta_{pv}}}$ at 10° and 20° AOA. The ratio of $C_{m_{\delta_{pv}}}$

in figure 14(a) to $C_{N_{\delta_{pv}}}$ in figure 14(c) is roughly 20 to 1. This ratio should be expected because the distance between the aircraft CG and the center of the vanes is approximately 20 ft, such that the primary normal force will occur at the vanes and produce a normalized pitching moment about the CG 20 times thereof. $C_{m_{\delta_{pv}}}$ showed the effects of plume pinching and $C_{N_{\delta_{pv}}}$ did not when the entire maneuver was initially analyzed (fig. 14(b)) because the primary information for each derivative is contained on different measurement signals. Pitch rate is the primary source of information for $C_{m_{\delta_{pv}}}$, and normal acceleration is the primary source of information for $C_{N_{\delta_{pv}}}$. Evidently, the noisy a_N signal was better matched by the small δ_{pv} deflections in figure 14(b). Again, as figure 14(c) shows, a nonlinearity exists between small and large δ_{pv} deflections (partially due to the amount of plume pinching), and the PID method found more benefit from the small-deflection portion on $C_{N_{\delta_{pv}}}$.

In addition, the accuracy of the real-time thrust measurement and calculation is important (ref. 45). Variations in this measurement or calculation from maneuver to maneuver will result in additional scatter in the estimates.

Stability Derivatives

Figure 15 shows the pitch-damping derivative C_{m_q} as a function of AOA. The flight-determined values are less negative than predicted from 10° to 20° AOA and at 60° AOA. Overall, the agreement is fairly good for this very difficult derivative to obtain from flight or wind-tunnel testing. The flight values show that the HARV is damped at 50° AOA, while the prediction shows it is undamped.

Figure 16(a) shows the subsonic longitudinal stability derivative C_{m_α}, where the flight values are compared with predicted values as a function of AOA. Below 30° and above 50° AOA there is excellent agreement. Both sets of values tend toward less stability between 20° and 30° AOA and more stability between 30° and 50° AOA. The largest disagreement occurs near 40° AOA, with the flight values showing much less stability than the predicted values.

Figure 16(b) compares flight-determined and predicted values for C_{N_α}. Overall, the agreement is very good, with small variations as to which value is larger below 40° AOA. Both flight and predicted values show that C_{N_α} is near zero at 60° AOA.

CONCLUSIONS

The subsonic longitudinal stability and control derivatives of the F-18 High Angle of Attack Research Vehicle (HARV) are determined from dynamic flight data using a maximum likelihood parameter

identification technique. The technique uses the linearized longitudinal aircraft equations of motion, accounting for thrust-vectoring terms as well as state and measurement noise. State noise is used to model the uncommanded forcing functions resulting from unsteady flows at high angles of attack. The aircraft is equipped with a thrust-vectoring system consisting of external nozzle postexit vanes and a research flight control system to control the integration of aerodynamic and propulsive controls. The actual coordination of vane motions to produce commanded pitch and yaw moments is managed by a mixer function within the research flight control system.

The flight maneuvers were initiated by an on-board excitation system that could somewhat modify the controls laws and allow for single-surface inputs. The independent inputs were ideal for parameter identification by eliminating correlations between control variables and state variables caused by feedback from the high-gain control augmentation system. Four typical longitudinal maneuvers at 10°, 20°, 30°, and 40° angles of attack were described, highlighting variations in doublet amplitude and aircraft response level. Also observed was the problem of opposing vane interference during vane doublets, causing reductions in the effectiveness of the thrust-vectoring controls. A total of 25 maneuvers was analyzed, each featuring control doublets in elevator (δ_e), symmetric aileron (δ_{sa}), trailing-edge flap (δ_{TEF}), and pitch vane input (δ_{pv}). Subsonic longitudinal stability and control derivatives (C_{m_α}, $C_{m_{\delta_e}}$, $C_{m_{\delta_{sa}}}$, $C_{m_{\delta_{TEF}}}$, $C_{m_{\delta_{pv}}}$, C_{m_q}, C_{N_α}, $C_{N_{\delta_e}}$, $C_{N_{\delta_{sa}}}$, $C_{N_{\delta_{TEF}}}$, and $C_{N_{\delta_{pv}}}$) are estimated and plotted as functions of angle of attack.

Comparisons were made with laboratory cold-jet thrust-vectoring predictions and with a simulation based primarily on wind-tunnel data. Several coefficients compared quite well, including those due to symmetric aileron ($C_{m_{\delta_{sa}}}$, $C_{N_{\delta_{sa}}}$) and those due to angle of attack (C_{m_α}, C_{N_α}). The coefficients of normal force due to elevator ($C_{N_{\delta_e}}$) and pitching moment due to trailing-edge flap ($C_{m_{\delta_{TEF}}}$) did not compare well. Coefficients of pitch vane effectiveness ($C_{m_{\delta_{pv}}}$, $C_{N_{\delta_{pv}}}$) revealed reductions of 20 to 30 percent, resulting from opposing vane interactions.

REFERENCES

1. Chambers, J. R., "High-Angle-of-Attack Aerodynamics: Lessons Learned," AIAA-86-1774, June 1986.

2. Chambers, Joseph R., "High-Angle-of-Attack Technology: Progress and Challenges," in *High-Angle-of-Attack Technology - Volume 1*, NASA CP-3149 Part 1, May 1992, pp. 1–22. (Note: ITAR restricted. Distribution authorized to U.S. Government agencies and their contractors; other requests shall be referred to WL/FIMS, Wright-Patterson AFB, Ohio 45433-6503.)

3. Gilbert, William P. and Donald H. Gatlin, "Review of the NASA High-Alpha Technology Program," *High-Angle-of-Attack Technology - Volume 1*, NASA CP-3149 Part 1, May 1992, pp. 23–59.

4. Chambers, Joseph R., William P. Gilbert, and Luat T. Nguyen, eds., *High-Angle-of-Attack Technology - Volume 1*, NASA CP-3149 Part 1, May 1992.

5. Matheny, Neil W., compiler, *High-Angle-of-Attack Projects and Technology Conference*, vols. 1–4, NASA CP-3207, Apr. 1992.

6. Regenie, Victoria, compiler, *Fourth NASA High Alpha Conference*, vols. 1–4, NASA CP-10143, July 1994.

7. Meyn, Larry A., Wendy R. Lanser, and Kevin D. James, "Full-Scale High Angle-of-Attack Tests of an F/A-18," AIAA-92-2676, June 1992.

8. Pettit, Chris L., Dansen L. Brown, Michael P. Banford, and Ed Pendleton, "Full-Scale Wind-Tunnel Pressure Measurements of an F/A-18 Tail During Buffet," *Journal of Aircraft*, vol. 33, no. 6, Nov.–Dec. 1996, pp. 1148–1156.

9. Asbury, Scott C. and Francis J. Capone, *Multiaxis Thrust-Vectoring Characteristics of Model Representative of the F-18 High-Alpha Research Vehicle at Angles of Attack From 0° to 70°*, NASA TP-3531, Dec. 1995.

10. Erickson, Gary E., *Wind Tunnel Investigation of Vortex Flows on F/A-18 Configuration at Subsonic Through Transonic Speed*, NASA TP-3111, Dec. 1991.

11. Cummings, Russell M., Yehia M. Rizk, Lewis B. Schiff, and Neal M. Chaderjian, "Navier-Stokes Predictions of the Flowfield Around the F-18 (HARV) Wing and Fuselage at Large Incidence," AIAA-90-0099, Jan. 1990.

12. Rizk, Yehia M. and Ken Gee, "Unsteady Simulation of Viscous Flowfield Around F-18 Aircraft at Large Incidence," *Journal of Aircraft*, vol. 29, no. 6, Nov.–Dec. 1992, pp. 986–992.

13. Murman, Scott M., Lewis B. Schiff, and Yehia M. Rizk, "Numerical Simulation of the Flow About an F-18 Aircraft in the High-Alpha Regime," AIAA-93-3405, Aug. 1993.

14. Murman, Scott M., Yehia M. Rizk, and Lewis B. Schiff, "Coupled Numerical Simulation of the External and Engine Inlet Flows for the F-18 at Large Incidence," AIAA-92-2621, June 1992.

15. Ghaffari, Farhad, *Navier-Stokes, Flight, and Wind Tunnel Flow Analysis for the F/A-18 Aircraft*, NASA TP-3478, Dec. 1994.

16. Gilbert, William P., Luat T. Nguyen, and Joseph Gera, "Control Research in the NASA High-Alpha Technology Program," in AGARD-CP-465, *Aerodynamics of Combat Aircraft Control and of Ground Effects*, pp. 3-1–3-18.

17. Pahle, Joseph W., Bruce Powers, Victoria Regenie, Vince Chacon, Steve Degroote, and Steven Murnyak, *Research Flight-Control System Development for the F-18 High Alpha Research Vehicle*, NASA TM-104232, Apr. 1991.

18. Foster, John V., W. T. Bundick, and Joseph W. Pahle, "Controls for Agility Research in the NASA High-Alpha Technology Program," SAE 912148, Sept. 1991.

19. Davidson, John B., John V. Foster, Aaron J. Ostroff, Frederick J. Lallman, Patrick C. Murphy, Keith D. Hoffler, and Michael D. Messina, "Development of a Control Law Design Process Utilizing Advanced Synthesis Methods with Application to the NASA F-18 HARV," in *High-Angle-of-Attack Projects and Technology Conference*, vol. 4, NASA CP-3207, Apr. 1992, pp. 111–157. (Note: ITAR restricted. Distribution authorized to U.S. Government agencies and their contractors; other requests shall be referred to WL/FIMS, Wright-Patterson AFB, Ohio 45433-6503.)

20. Ostroff, Aaron J., Keith D. Hoffler, and Melissa S. Proffitt, *High-Alpha Research Vehicle (HARV) Longitudinal Controller: Design, Analyses, and Simulation Results*, NASA TP-3446, July 1994.

21. Bowers, Albion H., Joseph W. Pahle, R. Joseph Wilson, Bradley C. Flick, and Richard L. Rood, *An Overview of the NASA F-18 High Alpha Research Vehicle*, NASA TM-4772, Oct. 1992.

22. Fisher, David F., John H. Del Frate, and Fanny A. Zuniga, *Summary of In-Flight Flow Visualization Obtained From the NASA High Alpha Research Vehicle*, NASA TM-101734, Jan. 1991.

23. Fisher, David F., David M. Richwine, and Daniel W. Banks, *Surface Flow Visualization of Separated Flows on the Forebody of an F-18 Aircraft and Wind-Tunnel Model*, NASA TM-100436, May 1988. (Also available as AIAA-88-2112.)

24. Fisher, David F., John H. Del Frate, and David M. Richwine, *In-Flight Flow Visualization Characteristics of the NASA F-18 High Alpha Research Vehicle at High Angles of Attack*, NASA TM-4193, May 1990.

25. Fisher, David F., D. W. Banks, and David M. Richwine, *F-18 High Alpha Research Vehicle Surface Pressures: Initial In-Flight Results and Correlation With Flow Visualization and Wind-Tunnel Data*, NASA TM-101724, 1990.

26. Del Frate, John H., David F. Fisher, and Fanny A. Zuniga, *In-Flight Flow Visualization With Pressure Measurements at Low Speeds on the NASA F-18 High Alpha Research Vehicle*, NASA TM-101726, 1990 (also presented at AGARD Vortex Flow Aerodynamics Conference, Scheveningen, Netherlands, Oct. 1–4, 1990).

27. Richwine, David M. and David F. Fisher, *In-Flight Leading-Edge Extension Vortex Flow-Field Survey Measurements on an F-18 Aircraft at High Angle of Attack*, NASA TM-4398, 1992. (Also available as AIAA-91-3248 using color reproduction.)

28. Shah, Gautam H., "Wind Tunnel Investigation of Aerodynamic and Tail Buffet Characteristics of Leading-Edge Extension Modifications to the F/A-18," AIAA-91-2889, Aug. 1991.

29. Lee, B. H. K. and F. C. Tang, "Characteristics of the Surface Pressures on a F/A-18 Vertical Fin Due to Buffet," *Journal of Aircraft*, vol. 31, no. 1, Jan.–Feb. 1994, pp. 228–235.

30. Meyn, Larry A. and Kevin D. James, "Full-Scale Wind-Tunnel Studies of F/A-18 Tail Buffet," *Journal of Aircraft*, vol. 33, no. 3, May–June 1996, pp. 589–595.

31. Gee, Ken, Scott M. Murman, and Lewis B. Schiff, "Computation of F/A-18 Tail Buffet," *Journal of Aircraft*, vol. 33, no. 6, Nov.–Dec. 1996, pp. 1181–1189.

32. Klein, Vladislav, Thomas P. Ratvasky, and Brent R. Cobleigh, *Aerodynamic Parameters of High-Angle-of-Attack Research Vehicle (HARV) Estimated From Flight Data*, NASA TM-102692, Aug. 1990.

33. Klein, Vladislav, "Aerodynamic Characteristics of High-Angle-of-Attack Research Vehicle (HARV) Determined From Flight Data," in *High-Angle-of-Attack Technology - Volume 1*, NASA CP-3149 part 1, May 1992, pp. 265–278.

34. Iliff, Kenneth W. and Kon-Sheng Charles Wang, *Extraction of Lateral-Directional Stability and Control Derivatives for the Basic F-18 Aircraft at High Angles of Attack*, NASA TM-4786, Feb. 1997.

35. Murri, Daniel G., Robert T. Biedron, Gary E. Erickson, Frank L. Jordan, Jr., and Keith D. Hoffler, "Development of Actuated Forebody Strake Controls for the F-18 High Alpha Research Vehicle," in *High-Angle-of-Attack Technology - Volume 1*, NASA CP-3149 part 1, May 1992, pp. 335–380.

36. Murri, Daniel G., Gautam H. Shah, Daniel J. DiCarlo, and Todd W. Trilling, "Actuated Forebody Strake Controls for the F-18 High-Alpha Research Vehicle," *Journal of Aircraft*, vol. 32, no. 3, May–June 1995, pp. 555–562. (Also available as AIAA-93-3675, Aug. 1993.)

37. Regenie, Victoria, Donald Gatlin, Robert Kempel, and Neil Matheny, *The F-18 High Alpha Research Vehicle: A High-Angle-of-Attack Testbed Aircraft*, NASA TM-104253, Sept. 1992. (Also available as AIAA-92-4121, Aug. 1992.)

38. Chacon, Vince, Joseph W. Pahle, and Victoria A. Regenie, *Validation of the F-18 High Alpha Research Vehicle Flight Control and Avionics Systems Modifications*, NASA TM-101723, Oct. 1990. (Also presented as paper for IEEE 9th Digital Avionics Systems Conferences, Virginia Beach, Virginia, Oct. 15–18, 1990.)

39. Regenie, Victoria A., Michael Earls, Jeanette Le, and Michael Thomson, *Experience With Ada on the F-18 High Alpha Research Vehicle Flight Test Program*, NASA TM-104259, Oct. 1992.

40. Iliff, Kenneth W. and Richard E. Maine, *Practical Aspects of Using a Maximum Likelihood Estimation Method to Extract Stability and Control Derivatives From Flight Data*, NASA TN D-8209, Apr. 1976.

41. Bowers, Albion H. and Joseph W. Pahle, *Thrust Vectoring on the NASA F-18 High Alpha Research Vehicle*, NASA TM-4771, Nov. 1996.

42. Bowers, Albion H., Gregory K. Noffz, Sue B. Grafton, Mary L. Mason, and Lee R. Peron, *Multiaxis Thrust Vectoring Using Axisymmetric Nozzles and Postexit Vanes on an F/A-18 Configuration Vehicle*, NASA TM-101741, May 1991. (Also available in NASA CP-3149, vol. 1, part 2, May 1992, pp. 829–862.)

43. Mason, Mary L., Francis J. Capone, and Scott C. Asbury, *A Static Investigation of the Thrust Vectoring System of the F/A-18 High-Alpha Research Vehicle*, NASA TM-4359, June 1992.

44. Johnson, Steven A., *Aircraft Ground Test and Subscale Model Results of Axial Thrust Loss Caused by Thrust Vectoring Using Turning Vanes*, NASA TM-4341, Jan. 1992.

45. Ray, Ronald J., *Evaluation of Various Thrust Calculation Techniques on an F404 Engine*, NASA TP-3001, Apr. 1990.

46. Peron, Lee R. and Thomas Carpenter, *Thrust Vectoring for Lateral-Directional Stability*, NASA CR-186016, 1992.

47. Heller, Michael J., "Theory and Implementation of the HARV/TVCS Mixer Predictor, NASA Contract NAS2-12661: NASA High Alpha Research Vehicle Thrust Vectoring Control System (HARV-TVCS)," Report HARV-MJH-12, McDonnell Aircraft Co., McDonnell Douglas Corp., St. Louis, Missouri, Aug. 10, 1989.

48. Bundick, W. Thomas, Joseph W. Pahle, Jessie C. Yeager, and Fred L. Beissner, Jr., *Design of a Mixer for the Thrust-Vectoring System on the High-Alpha Research Vehicle*, NASA TM-110228, June 1996.

49. Moes, Timothy R. and Stephen A. Whitmore, *A Preliminary Look at Techniques Used to Obtain Airdata From Flight at High Angles of Attack*, NASA TM-101729, Dec. 1990.

50. Whitmore, Stephen A., Timothy R. Moes, and Terry J. Larson, *Preliminary Results From a Subsonic High Angle-of-Attack Flush Airdata Sensing (HI-FADS) System: Design, Calibration, and Flight Test Evaluation*, NASA TM-101713, Jan. 1990. (Also available as AIAA-90-0232, Jan. 1990.)

51. Whitmore, Stephen A, *Development of a Pneumatic High-Angle-of-Attack Flush Airdata Sensing (HI-FADS) System*, NASA TM-104241, Nov. 1991.

52. Moes, Timothy R., Stephen A. Whitmore, and Frank L. Jordan, *Flight and Wind-Tunnel Calibrations of a Flush Airdata Sensor at High Angles of Attack and Sideslip and at Supersonic Mach Numbers*, NASA TM-104265, 1993. (Also presented as AIAA-93-1017, Feb. 1993.)

53. Richwine, David M., Robert E. Curry, and Gene V. Tracy, *A Smoke Generator System for Aerodynamic Flight Research*, NASA TM-4137, Sept. 1989.

54. Yuhas, Andrew J., Ronald J. Ray, Richard R. Burley, William G. Steenken, Leon Lechtenberg, and Don Thornton, *Design and Development of an F/A-18 Inlet Distortion Rake: A Cost and Time Saving Solution*, NASA TM-4722, Oct. 1995.

55. Smith, C. Frederic, Steve D. Podleski, Wendy S. Barankiewicz, and Susan Z. Zeleznik, "Comparison of F/A-18A Inlet Flow Analyses with Flight Data part 1," *Journal of Aircraft*, vol. 33, no. 3, May–June 1996, pp. 457–462.

56. Smith, C. Frederic, Steve D. Podleski, Wendy S. Barankiewicz, and Susan Z. Zeleznik, "Comparison of F/A-18A Inlet Flow Analyses with Flight Data part 2," *Journal of Aircraft*, vol. 33, no. 3, May–June 1996, pp. 463–469.

57. Iliff, Kenneth W., Richard E. Maine, and Mary F. Shafer, *Subsonic Stability and Control Derivatives for an Unpowered, Remotely Piloted 3/8-Scale F-15 Airplane Model Obtained From Flight Test*, NASA TN D-8136, Jan. 1976.

58. Iliff, K. W., "Identification and Stochastic Control with Application to Flight Control in Turbulence," UCLA-ENG-7340, Ph.D. Dissertation, University of California Los Angeles, California, May 1973.

59. Maine, R. E. and K. W. Iliff, *Identification of Dynamic Systems*, AGARD-AG-300, vol. 2, Jan. 1985. (Also available as NASA RP-1138, Feb. 1985.)

60. Iliff, Kenneth W., "Identification and Stochastic Control of an Aircraft Flying in Turbulence," *Journal of Guidance and Control*, vol. 1, no. 2, Mar.–Apr. 1978, pp. 101–108.

61. Iliff, Kenneth W. and Lawrence W. Taylor, Jr., *Determination of Stability Derivatives From Flight Data Using a Newton-Raphson Minimization Technique*, NASA TN D-6579, Mar. 1972.

62. Maine, Richard E. and Kenneth W. Iliff, *Application of Parameter Estimation to Aircraft Stability and Control - The Output-Error Approach*, NASA RP-1168, June 1986.

63. Etkin, Bernard, *Dynamics of Flight—Stability and Control*, 2nd ed., John Wiley & Sons, New York, 1982.

64. Maine, Richard E. and Kenneth W. Iliff, *User's Manual for MMLE3, a General FORTRAN Program for Maximum Likelihood Parameter Estimation*, NASA TP-1563, Nov. 1980.

65. Weiss, Susanne, Holger Friehmelt, Ermin Plaetschke, and Detlef Rohlf, "X-31A System Identification Using Single-Surface Excitation at High Angles of Attack," *Journal of Aircraft*, vol. 33, no. 3, May–June 1996, pp. 485–490.

66. Anon., "F/A-18 Basic Aerodynamic Data," MDC A8575, McDonnell Aircraft Co., McDonnell Douglas Corp., St. Louis, Missouri, 1984.

67. Pelikan, R. J. and R. L. Swingle, "F/A-18 Stability and Control Data Report," vols. I and II, MDC A7247, Rev. B, McDonnell Aircraft Co., McDonnell Douglas Corp., St. Louis, Missouri, Nov. 1982.

Figure 1. F-18 HARV.

Aileron

Leading-edge flaps

Trailing-edge flap

Stabilator

21.6 ft

Leading-edge
extension (wing-
body strake

Speed
brake

Airdata boom

56 ft

Rudder

15.3 ft

10.5 ft

Wing area = 400 ft^2
MAC = 11.52 ft
Aspect ratio = 3.5
Stabilator area = 86.48 ft^2
Weight = 36,099 lb
(includes 60 percent
fuel condition of
6,480 lb)

37.4 ft

960825
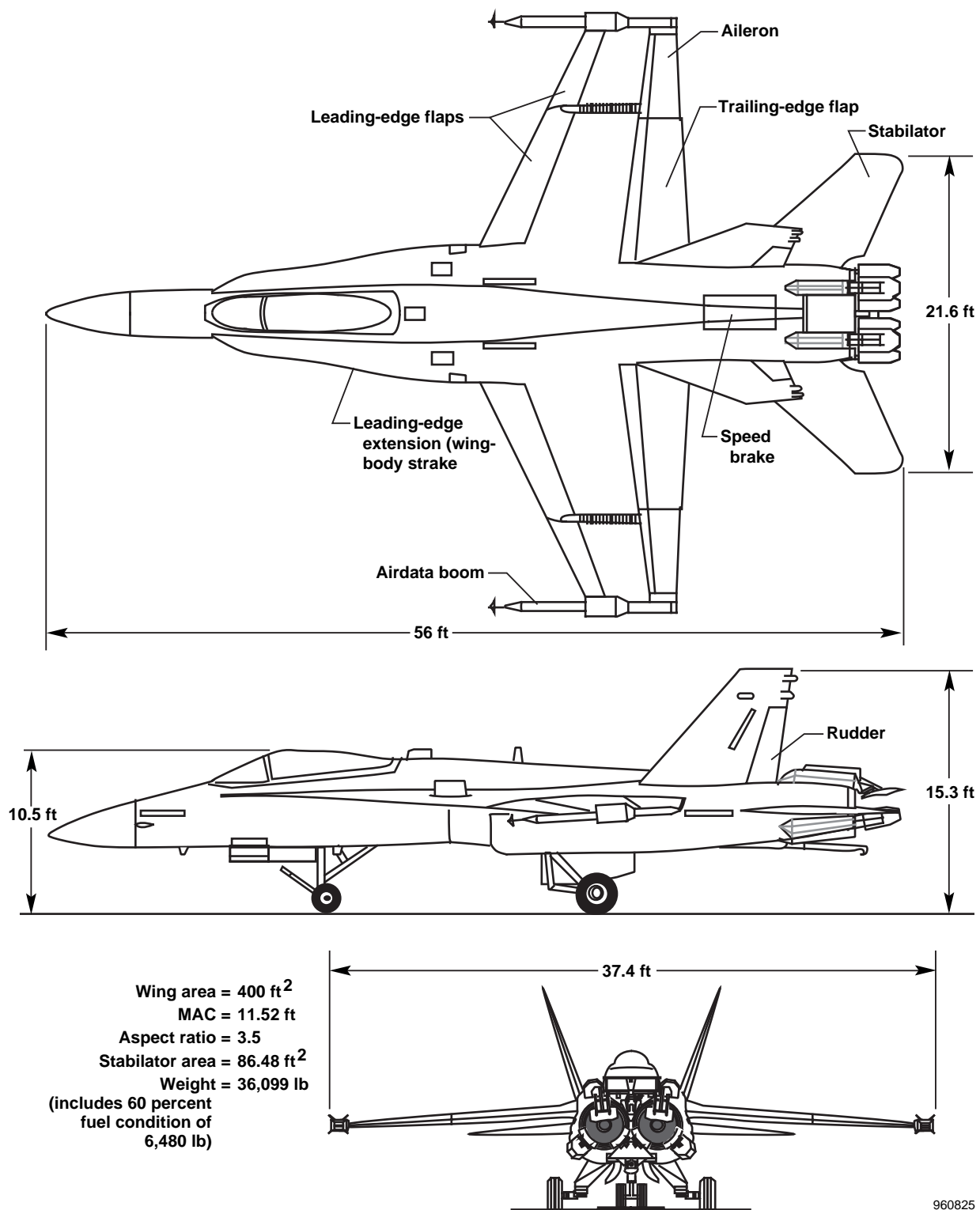
Figure 2. Three-view drawing of the F-18 HARV with major dimensions shown.

35

Figure 3. Hardware modification of the thrust-vectoring control system.

Vane position limits

10°

25°

Left engine vanes

5°

Upper vane

**Maximum
afterburner
nozzle, 348 in^2**

138.5˚

118˚

**Military power
nozzle, 220 in^2**

Inner vane

Outer vane

103.5˚

Radius = 36 in.

5.185 in.

9.120 in.

20 in.

20 in.

**Inner and
outer vanes**

Upper vane

12.591 in.

12.420 in.

15 in.

20 in.

Area = 263.64 in^2

Area = 358.76 in^2

910078
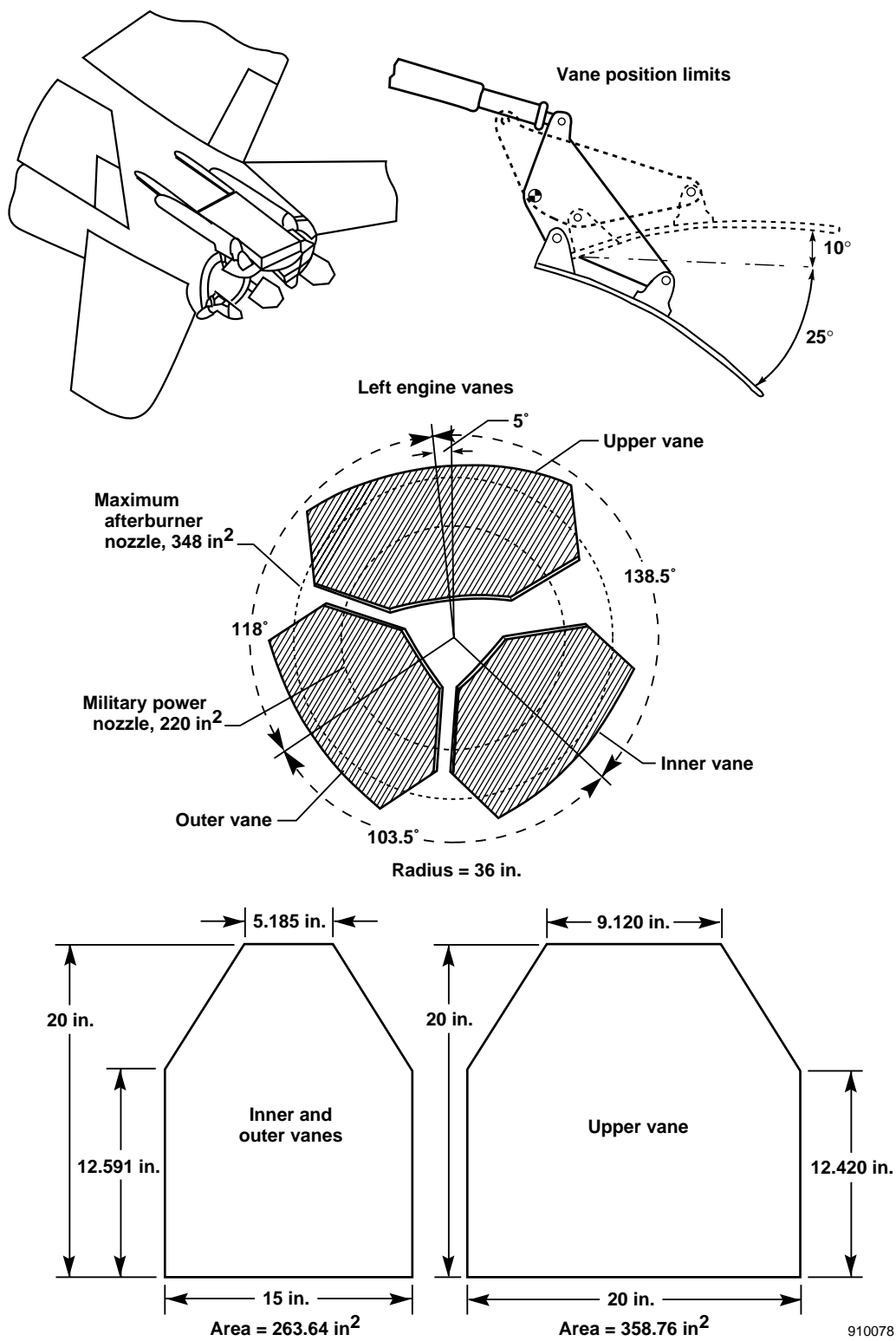
Figure 4. Four-view drawing of the TVCS.
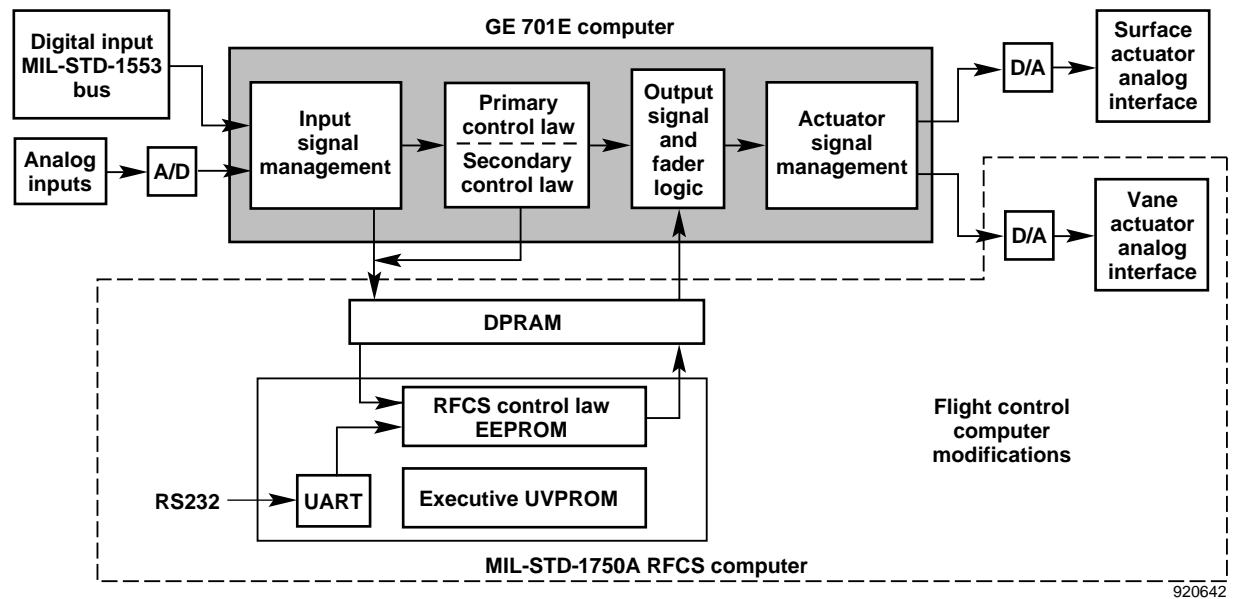
(a) The GE 701E and MIL-STD-1750A computers.
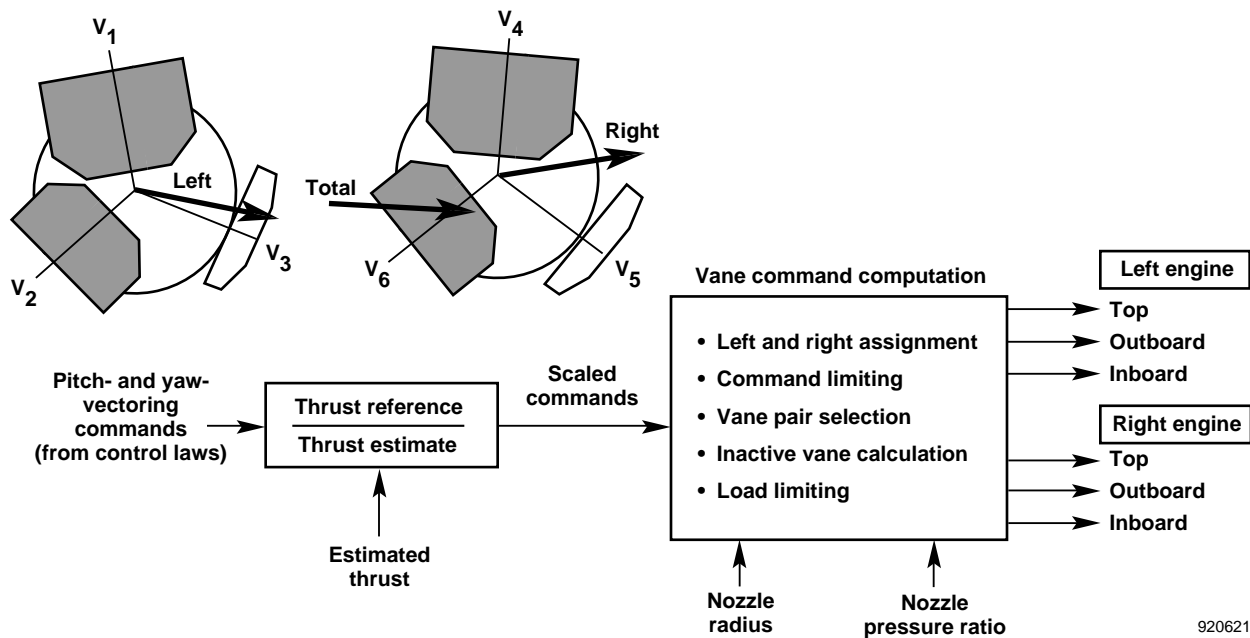
(b) Simplified thrust vane mixer function.

Figure 5. HARV research flight control system computer architecture.
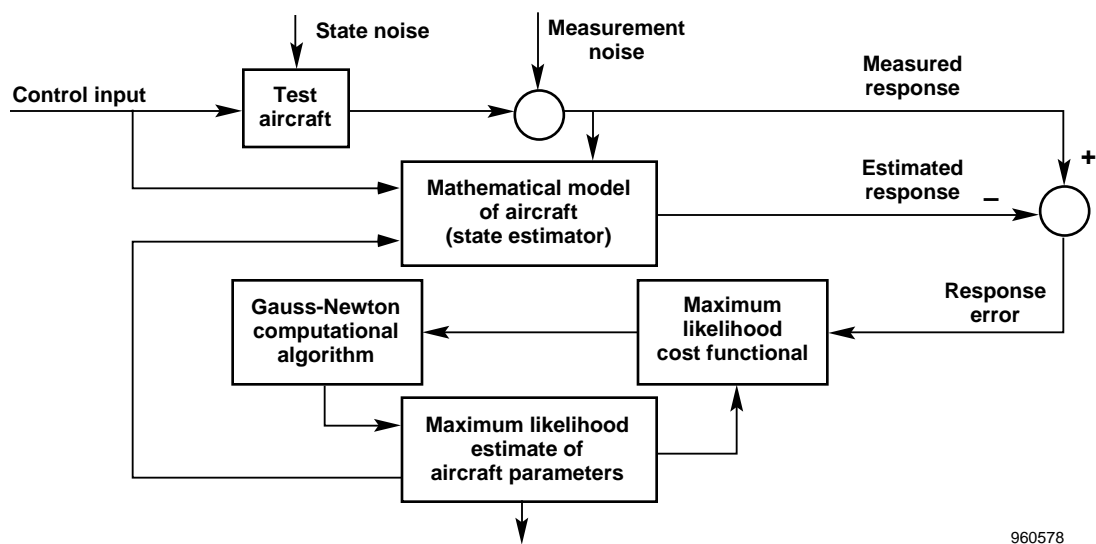
Figure 6. Maximum likelihood estimation concept with state and measurement noise.
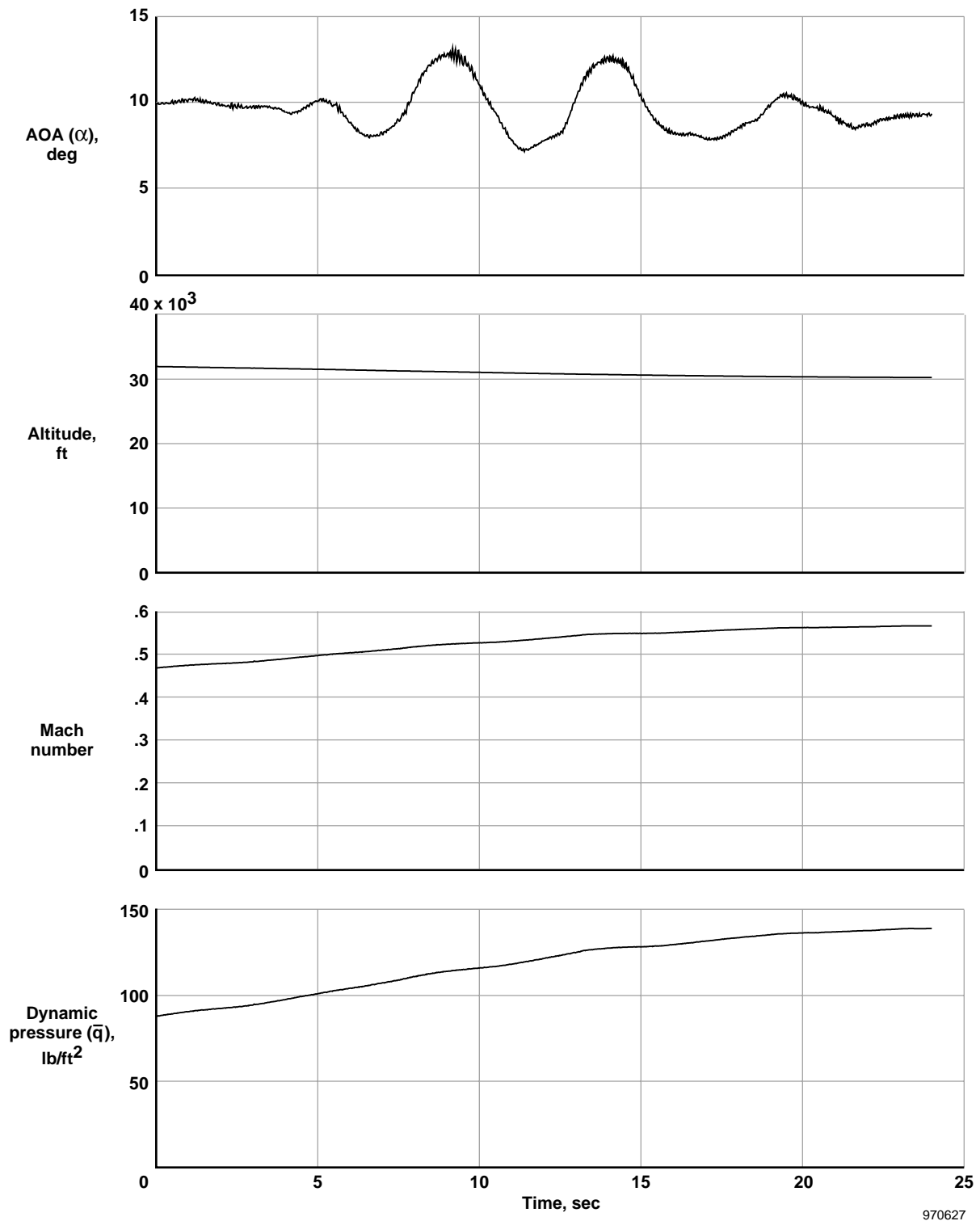
(a) Part 1 of 5.

Figure 7. Time history data from a typical 10° AOA subsonic longitudinal stability and control maneuver.

40
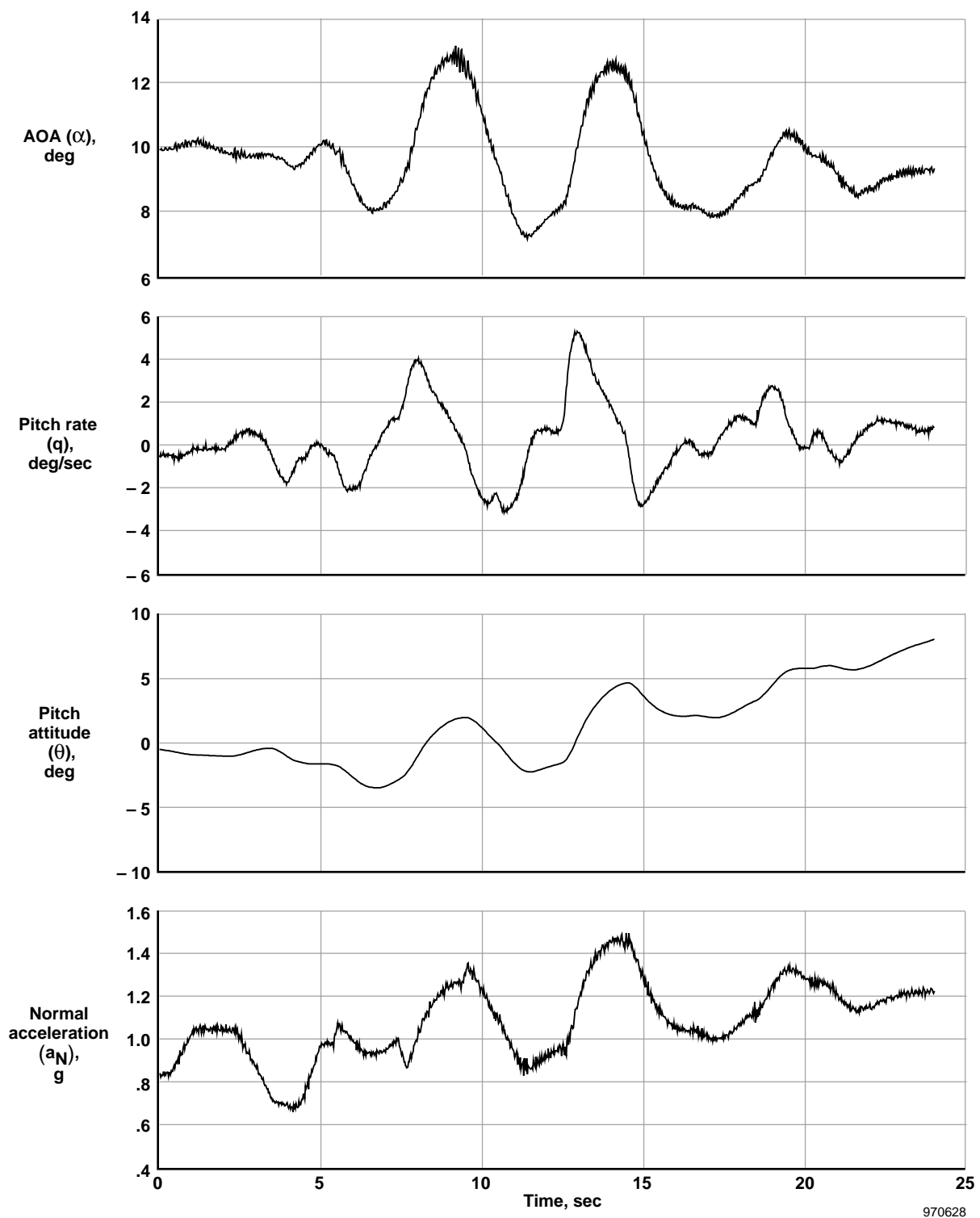
(b) Part 2 of 5.

Figure 7. Continued.

970628
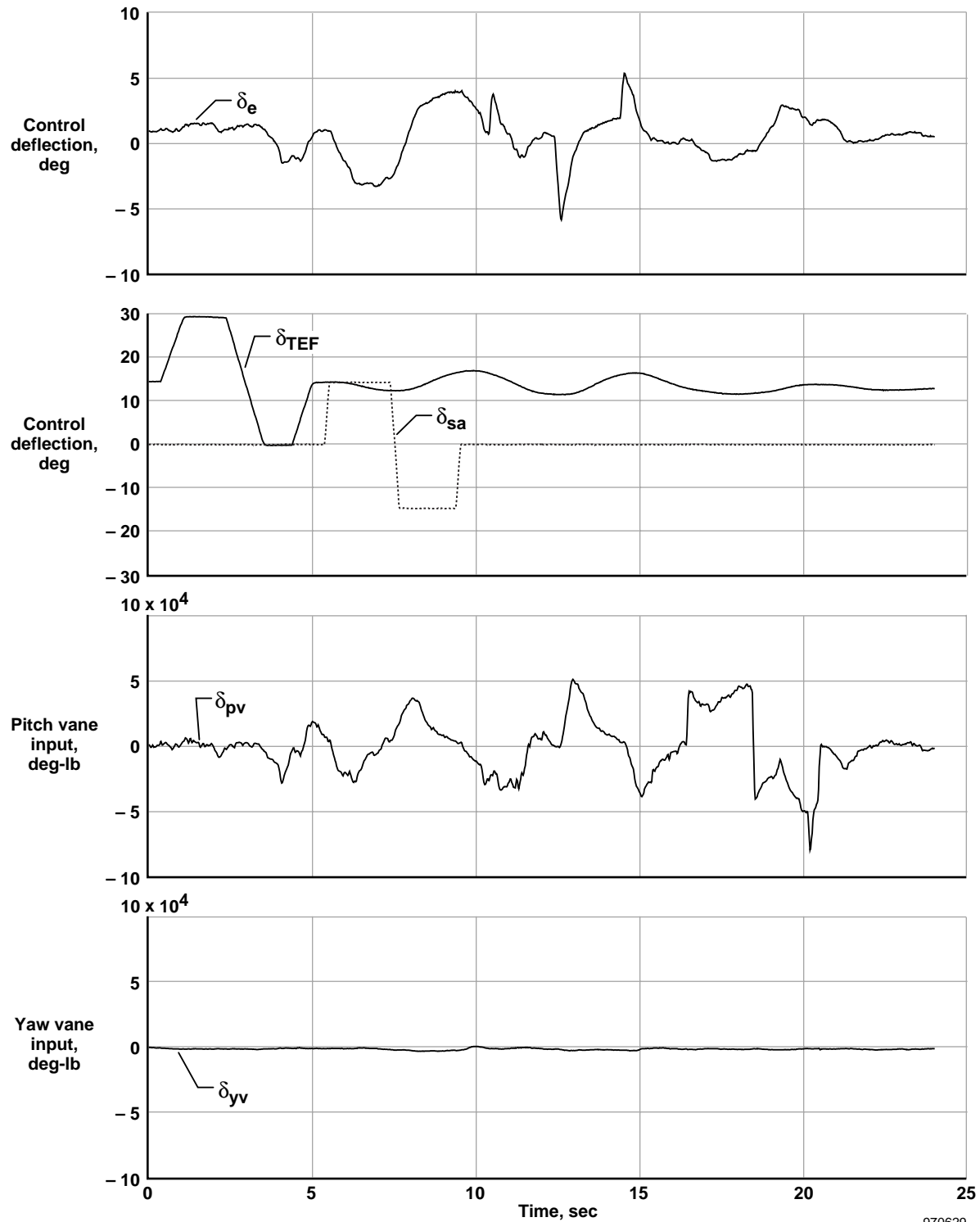
(c) Part 3 of 5.

Figure 7. Continued.

42
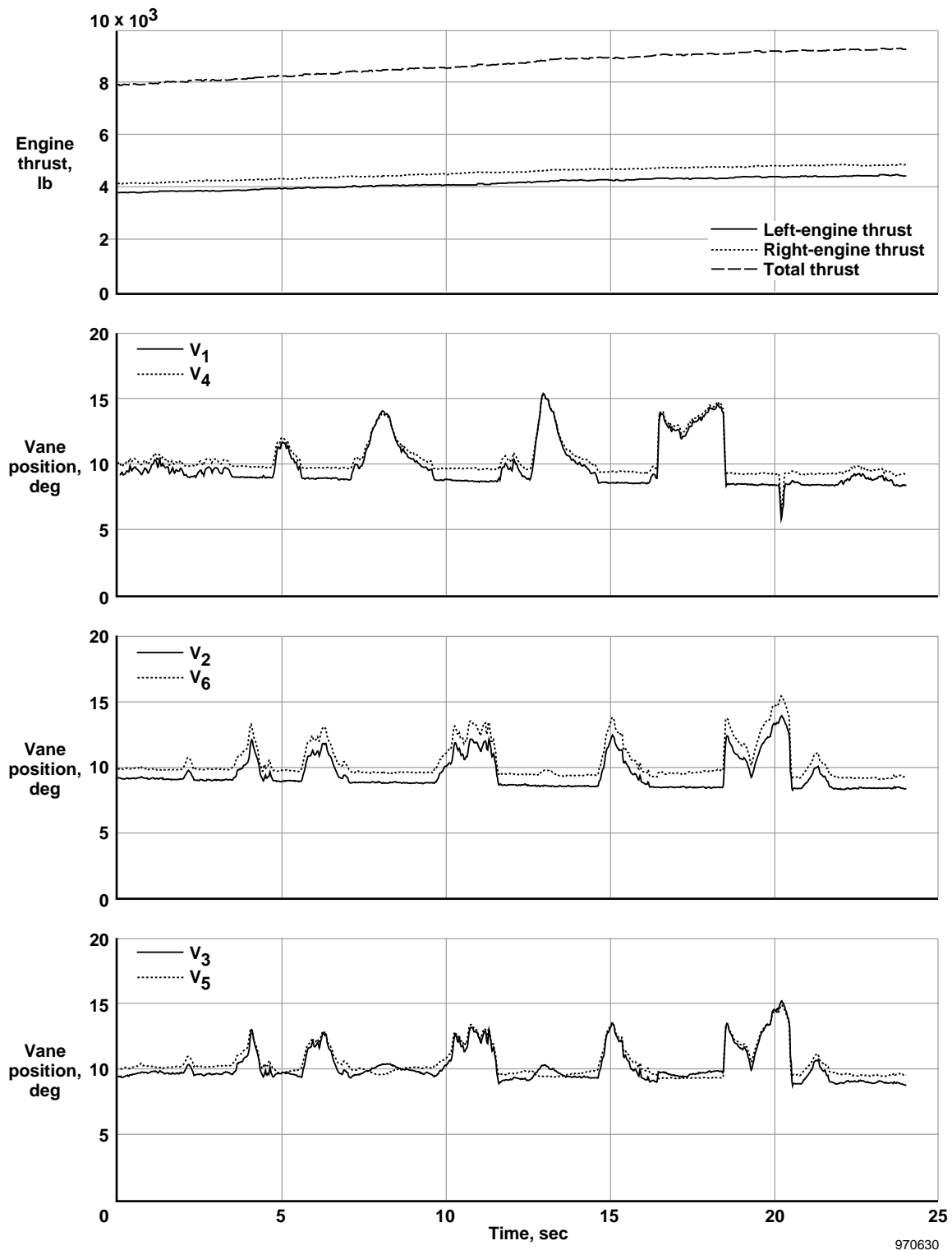
(d) Part 4 of 5.

Figure 7. Continued.
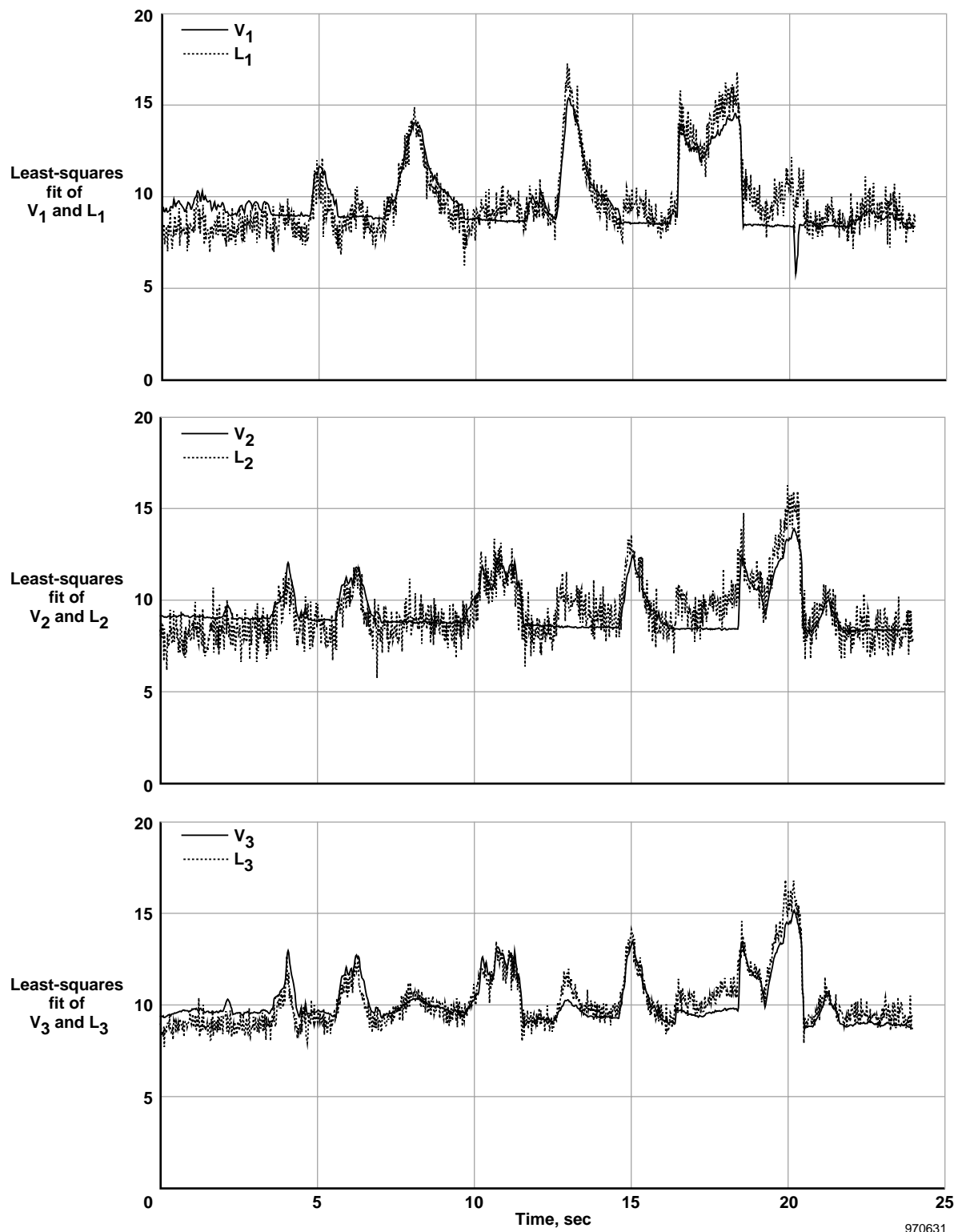
(e) Part 5 of 5.

Figure 7. Concluded.

970631

44
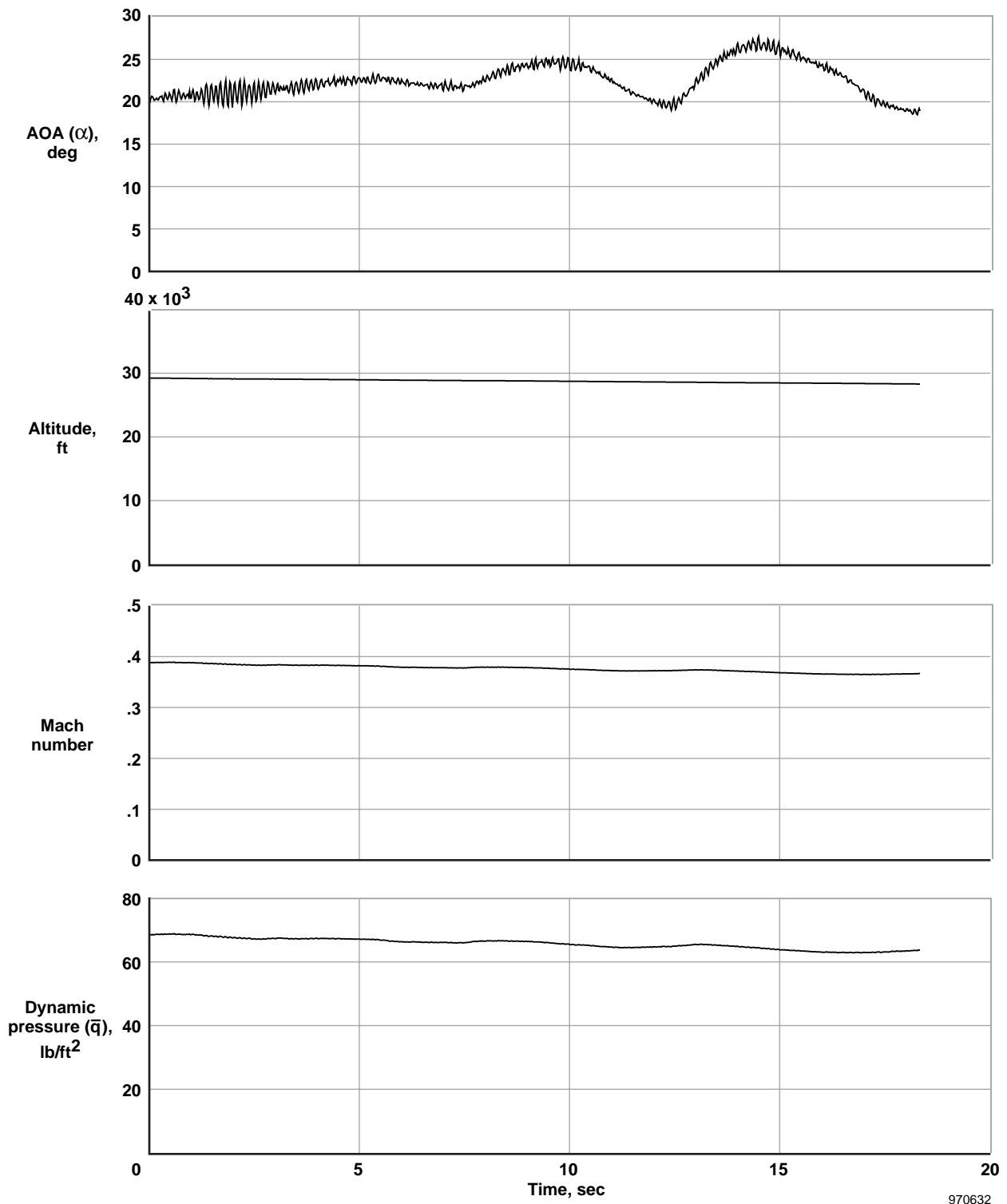
(a) Part 1 of 5.

Figure 8. Time history data from a typical 20° AOA subsonic longitudinal stability and control maneuver.
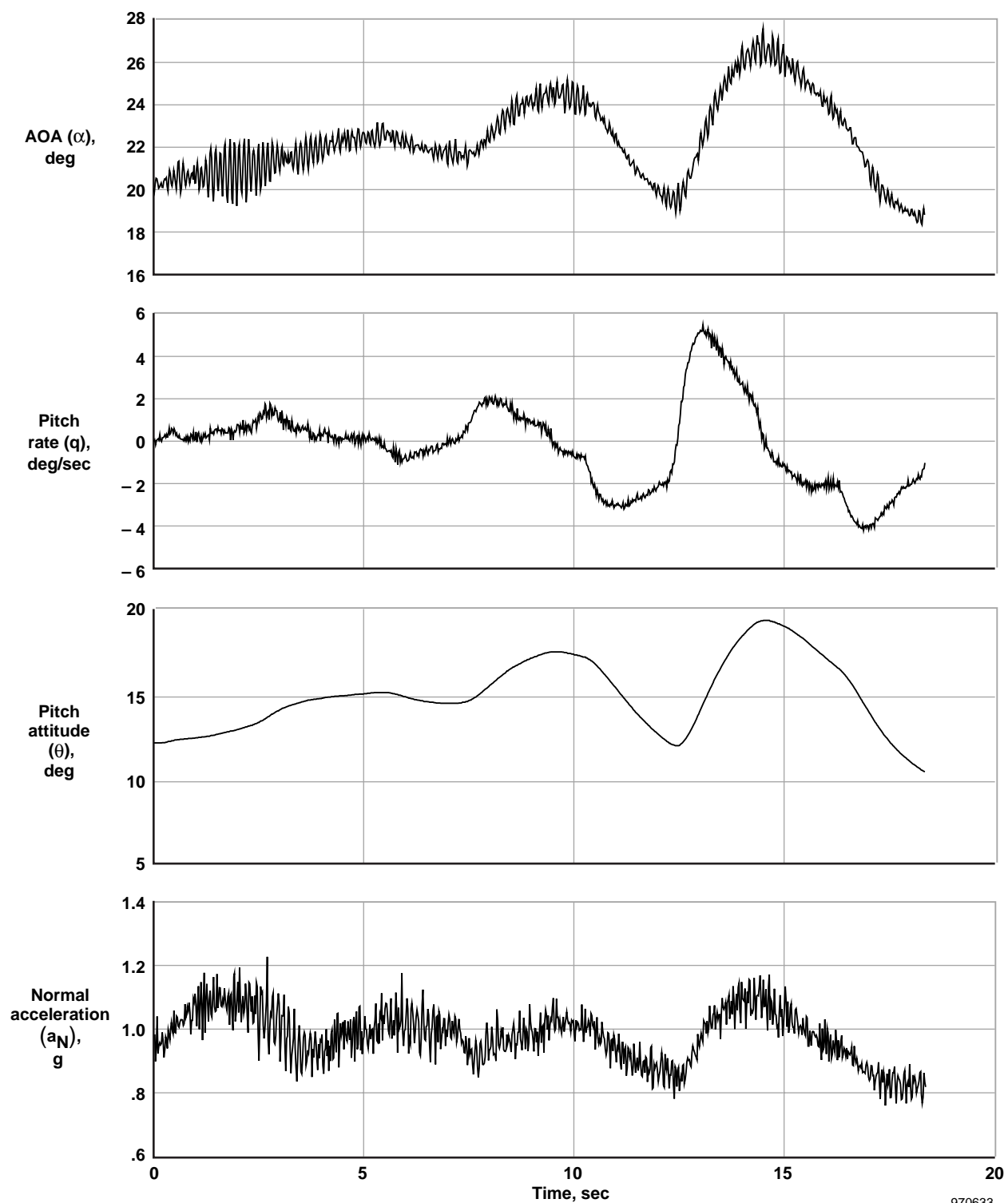
(b) Part 2 of 5.

Figure 8. Continued.
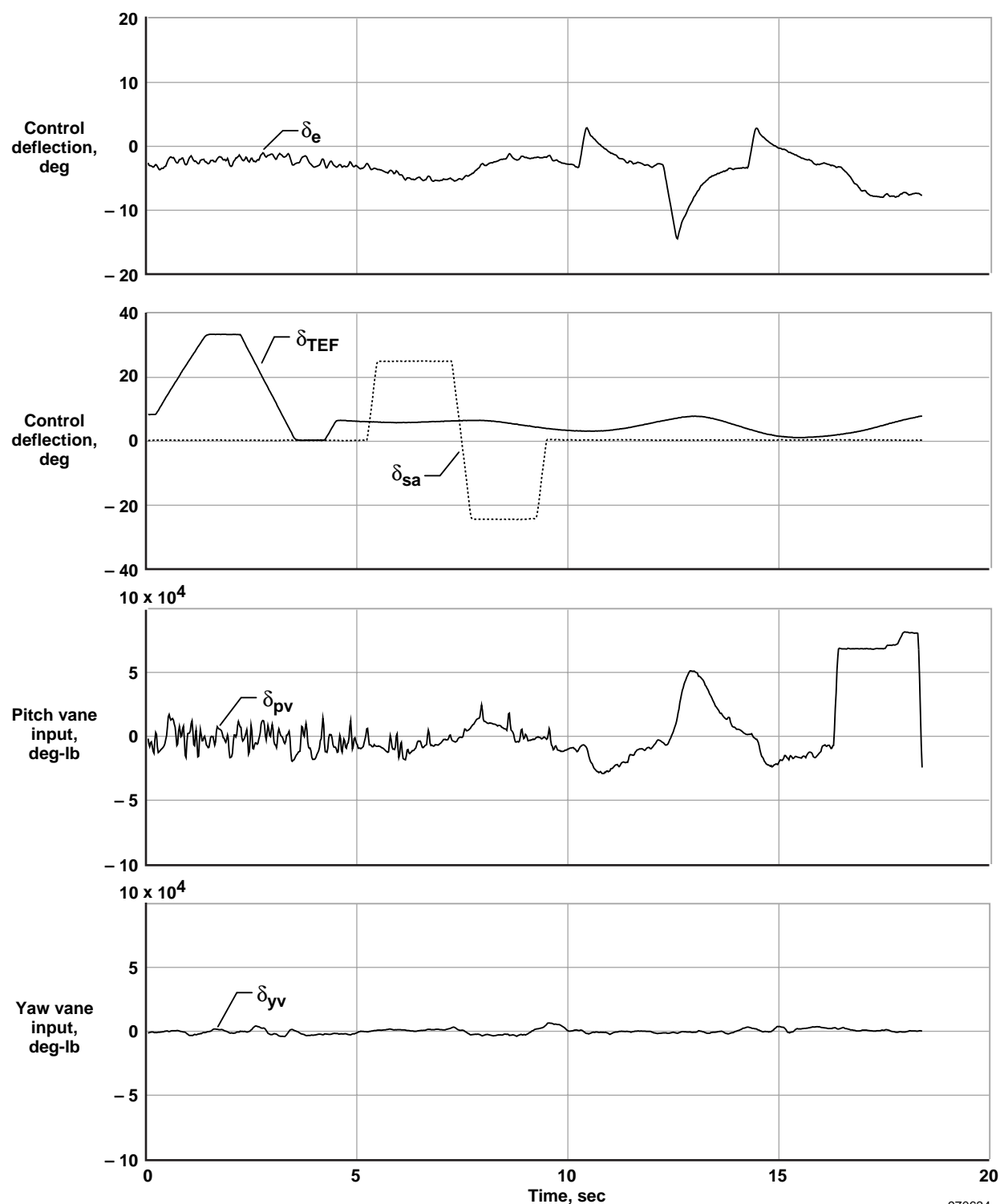
(c) Part 3 of 5.

Figure 8. Continued.
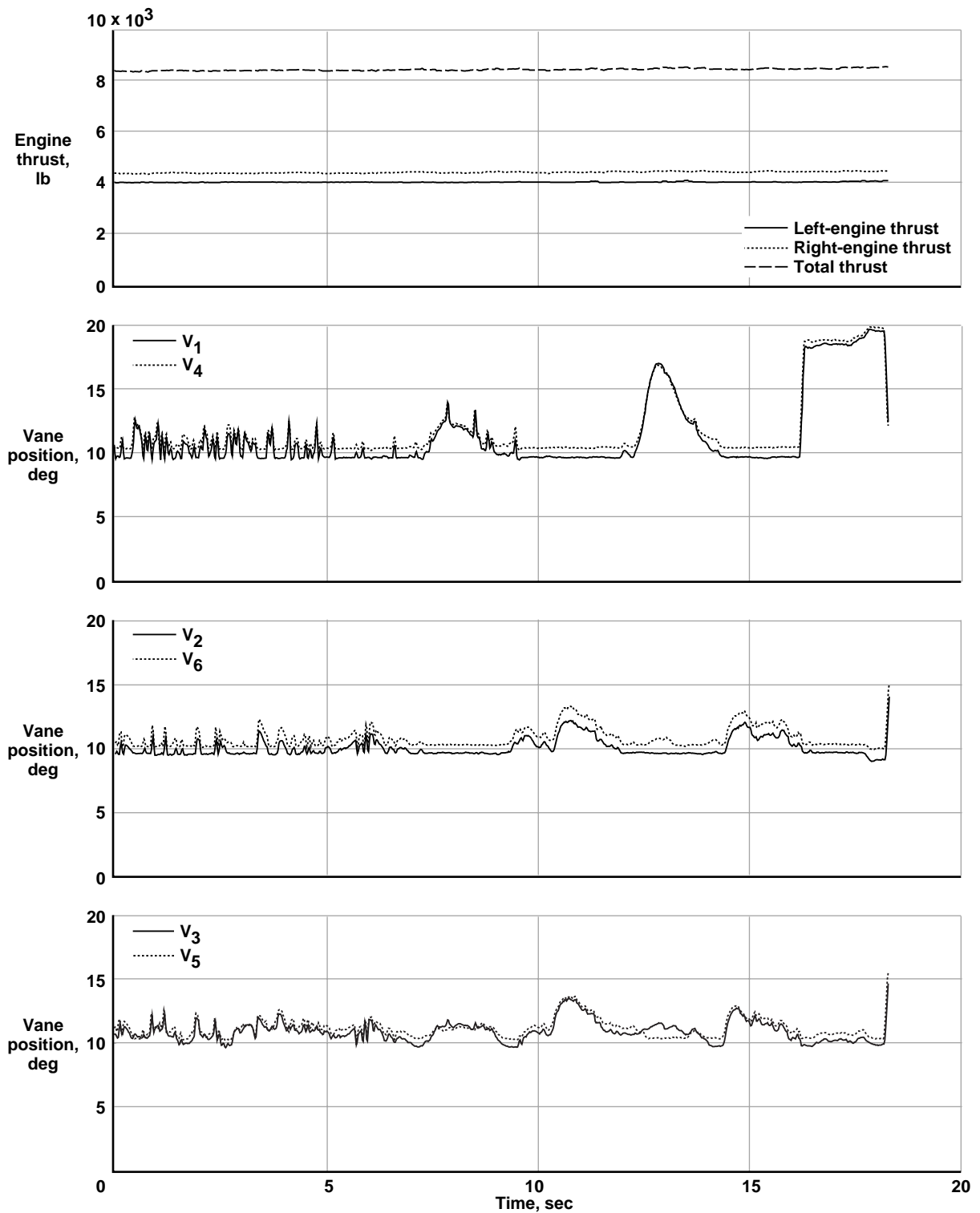
(d) Part 4 of 5.

Figure 8. Continued.
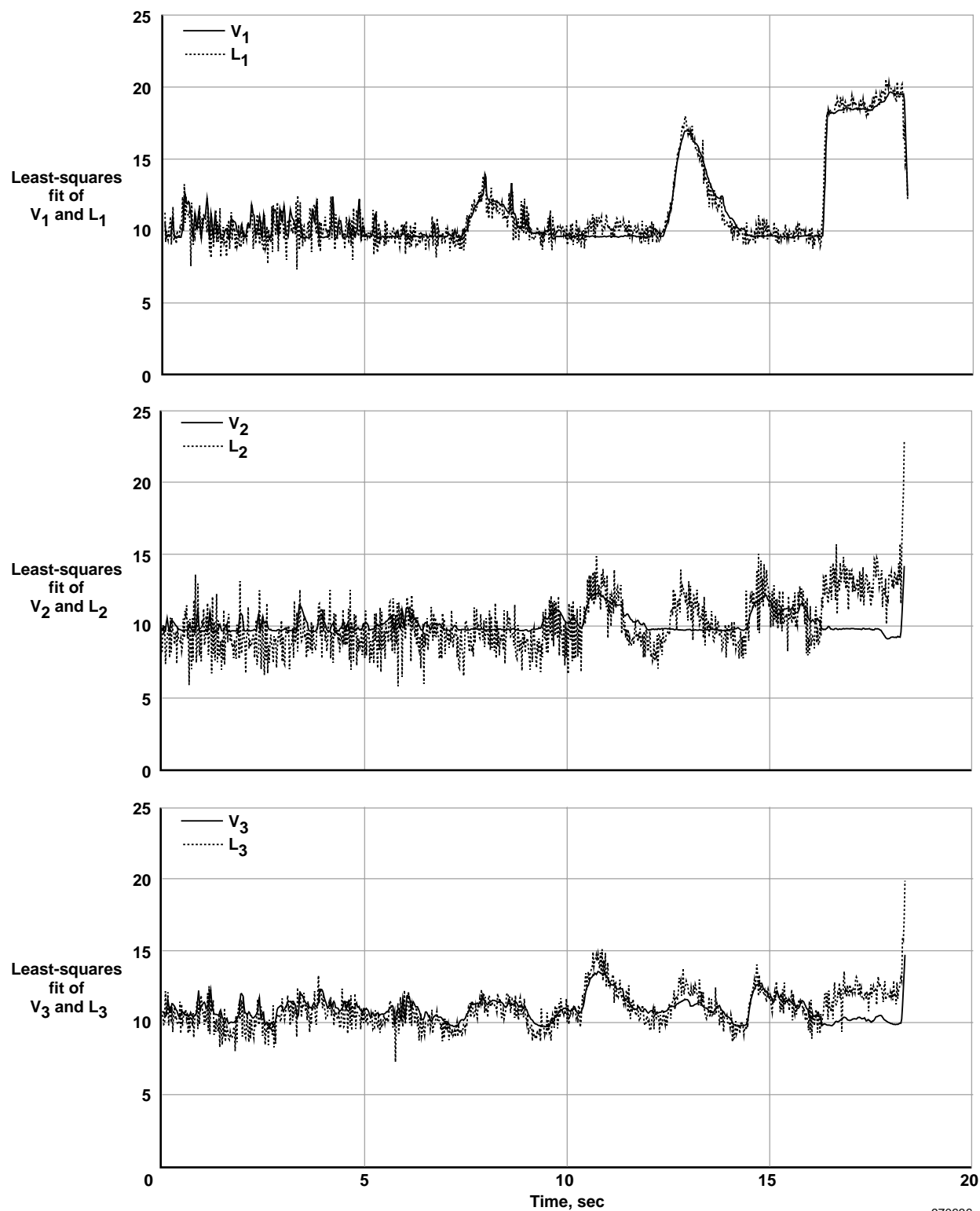
970635

(e) Part 5 of 5.

Figure 8. Concluded.

49
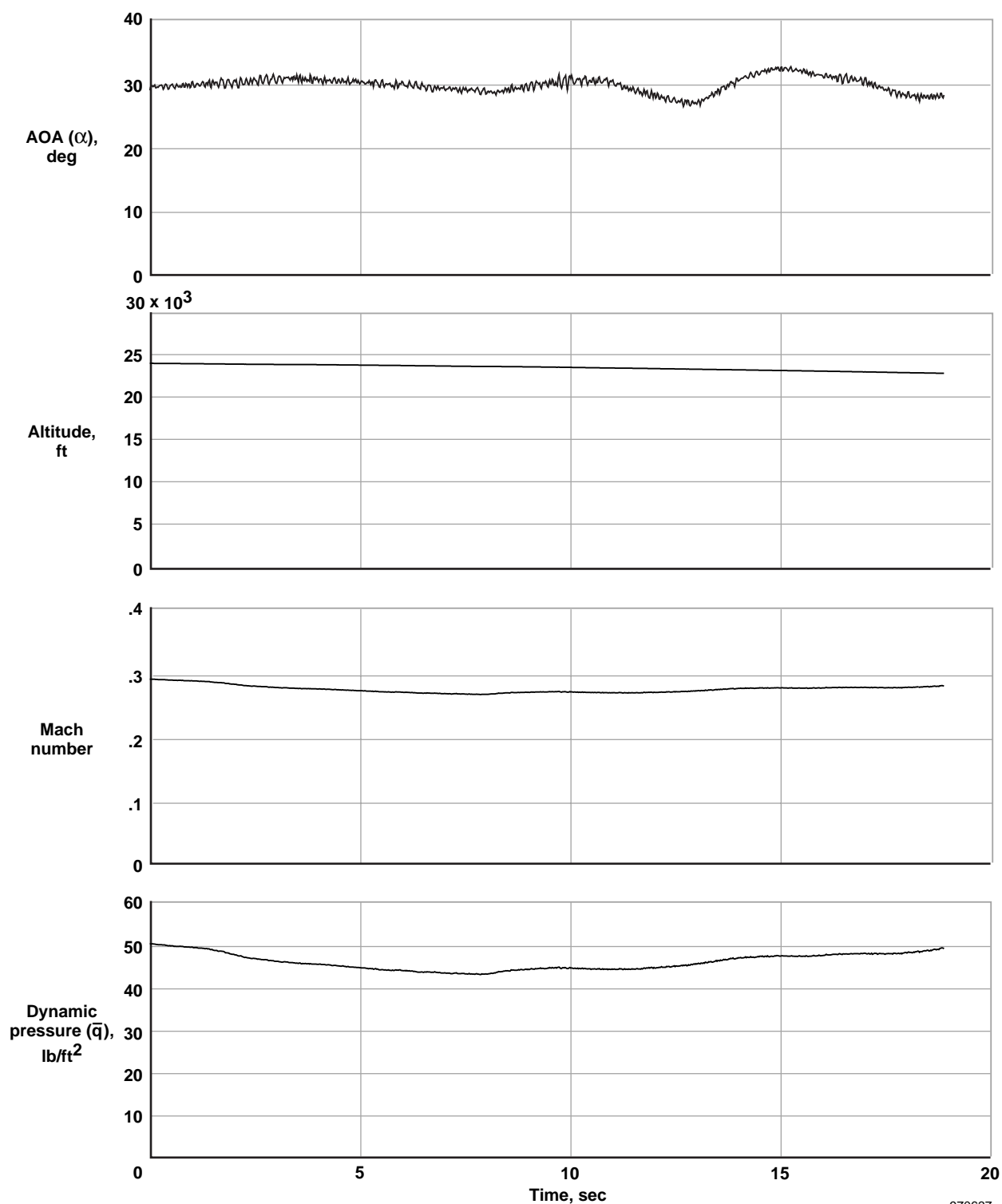
(a) Part 1 of 5.

Figure 9. Time history data from a typical 30° AOA subsonic longitudinal stability and control maneuver.

50
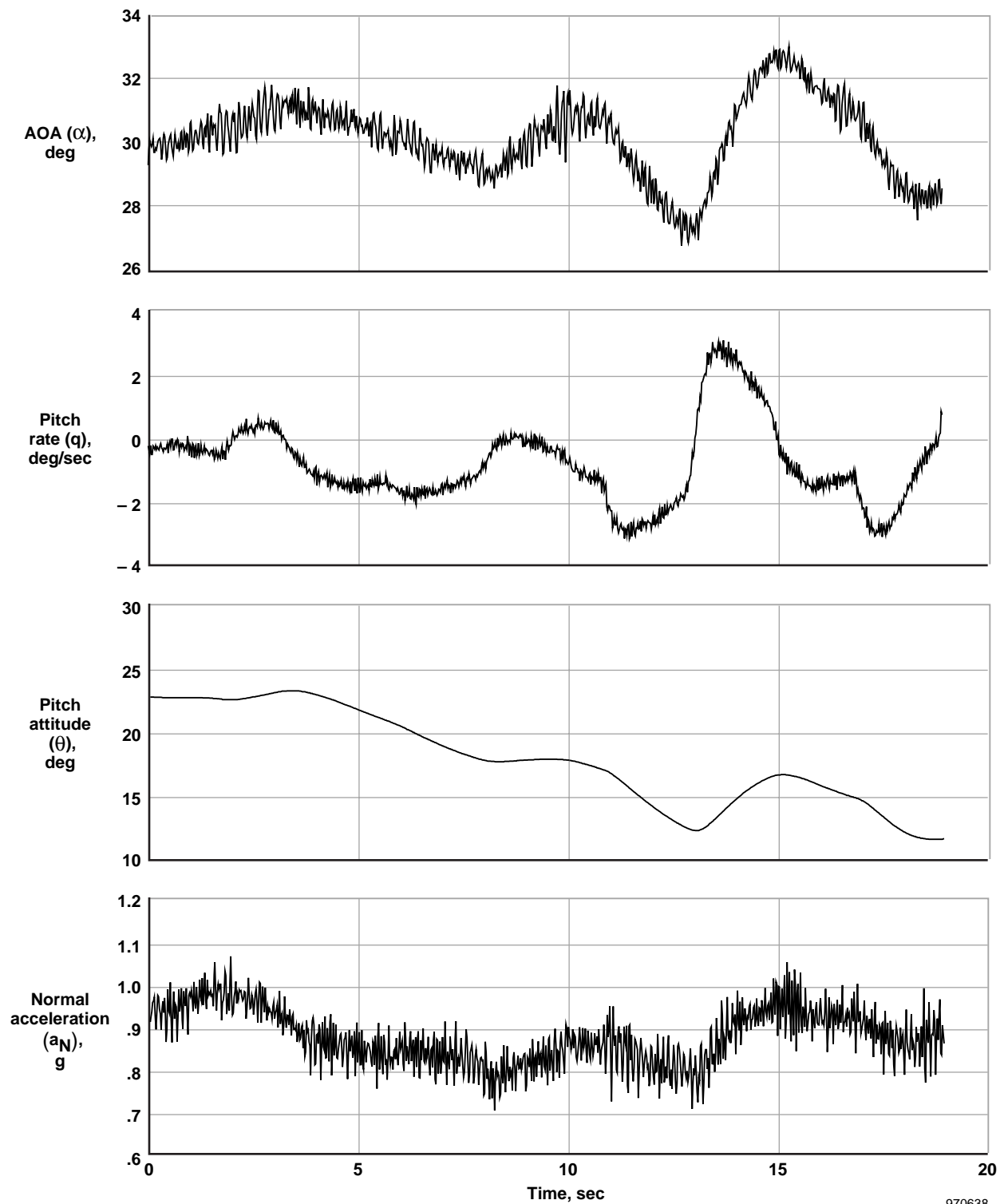
(b) Part 2 of 5.

Figure 9. Continued.
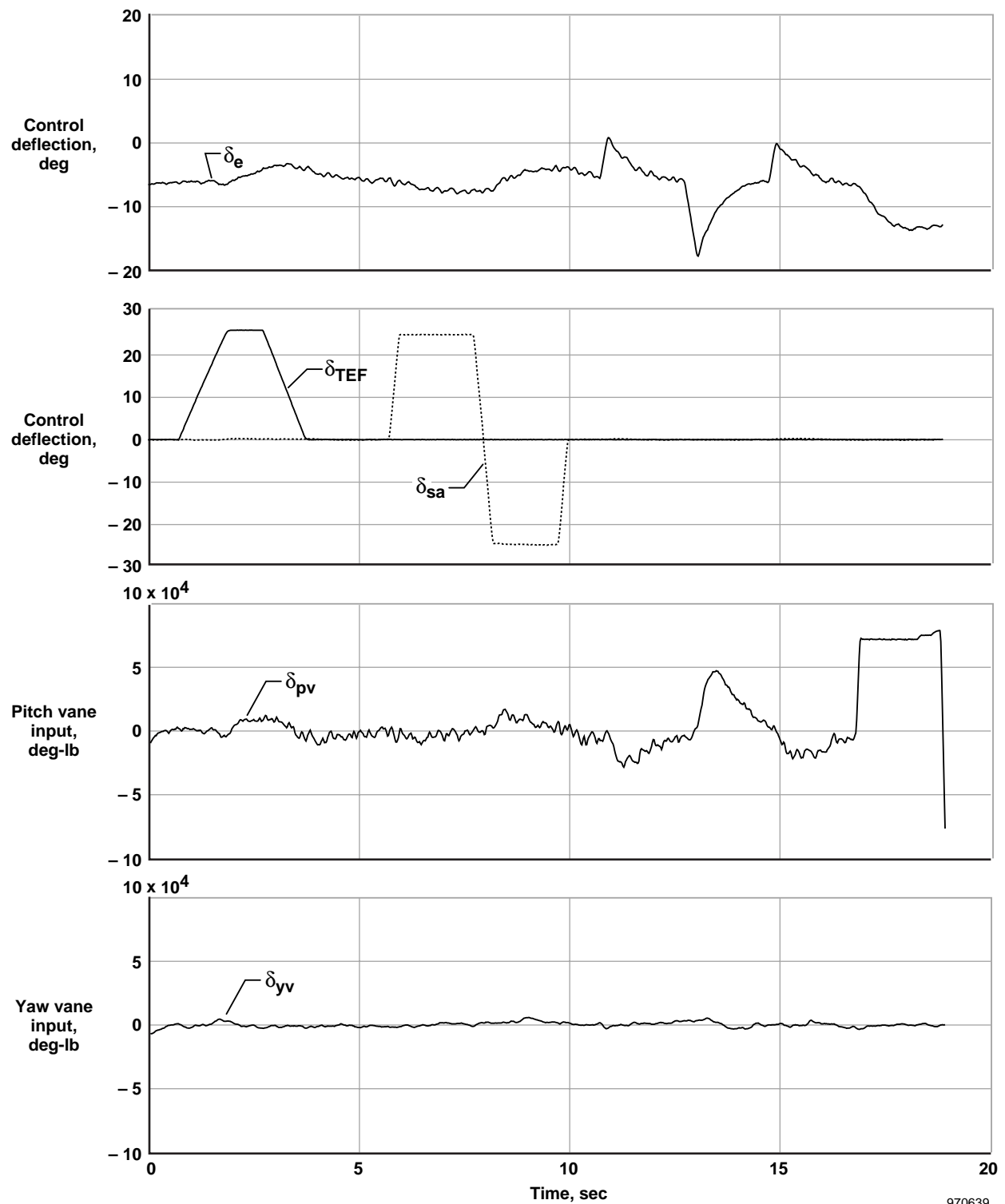
970638

(c) Part 3 of 5.

Figure 9. Continued.

970639

52
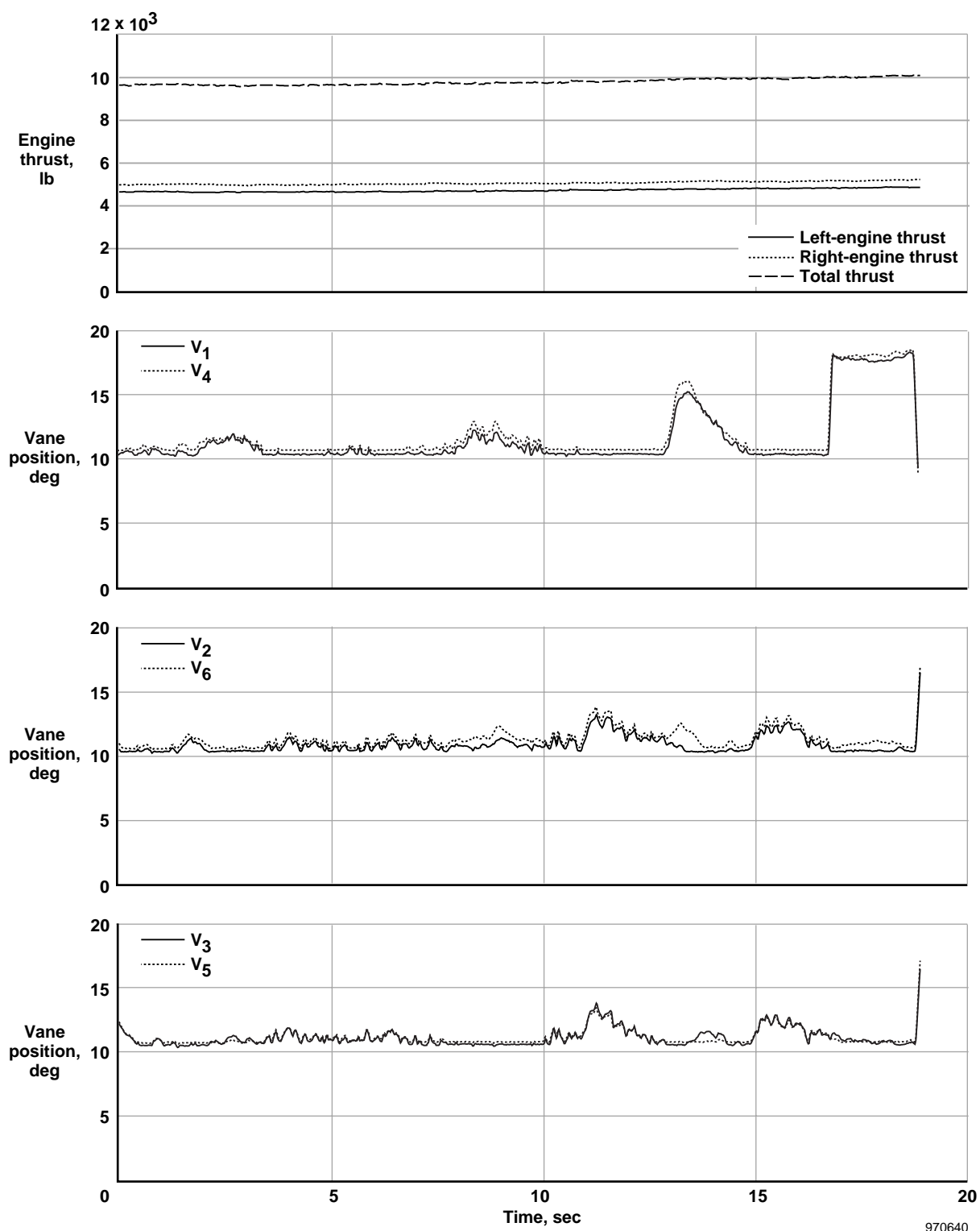
(d) Part 4 of 5.

Figure 9. Continued.
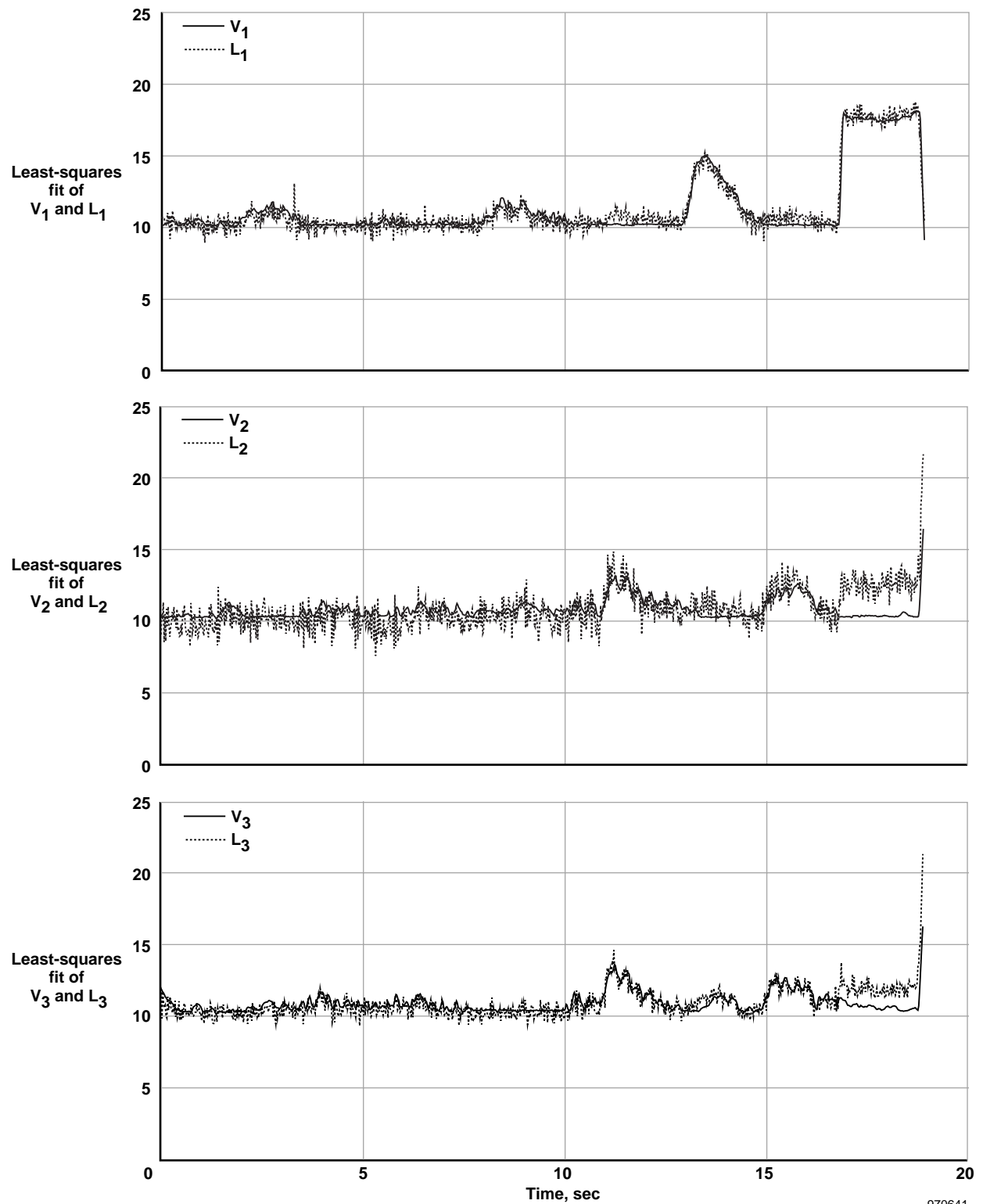
(e) Part 5 of 5.

Figure 9. Concluded.
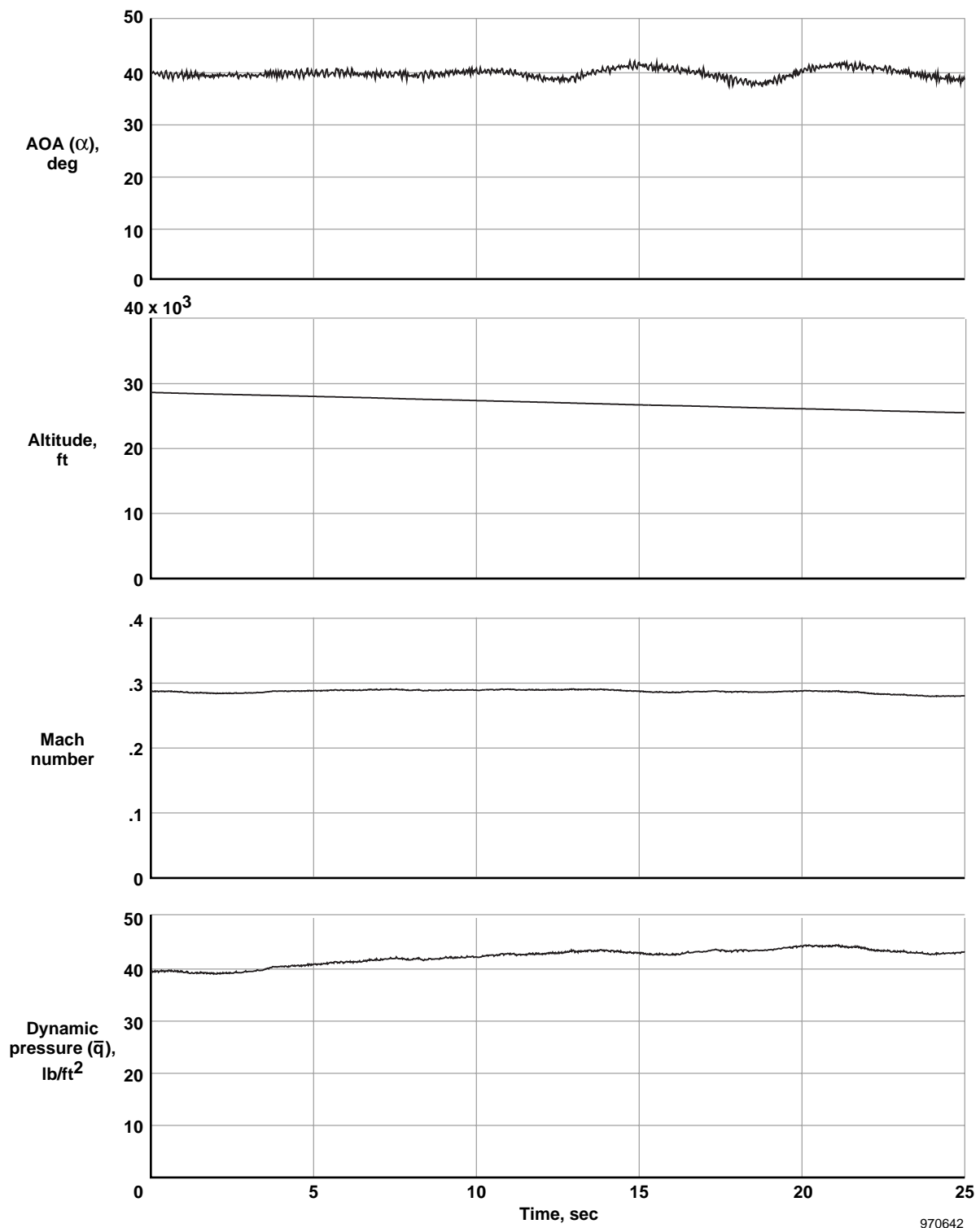
970641

(a) Part 1 of 5.

Figure 10. Time history data from a typical 40° AOA subsonic longitudinal stability and control maneuver.
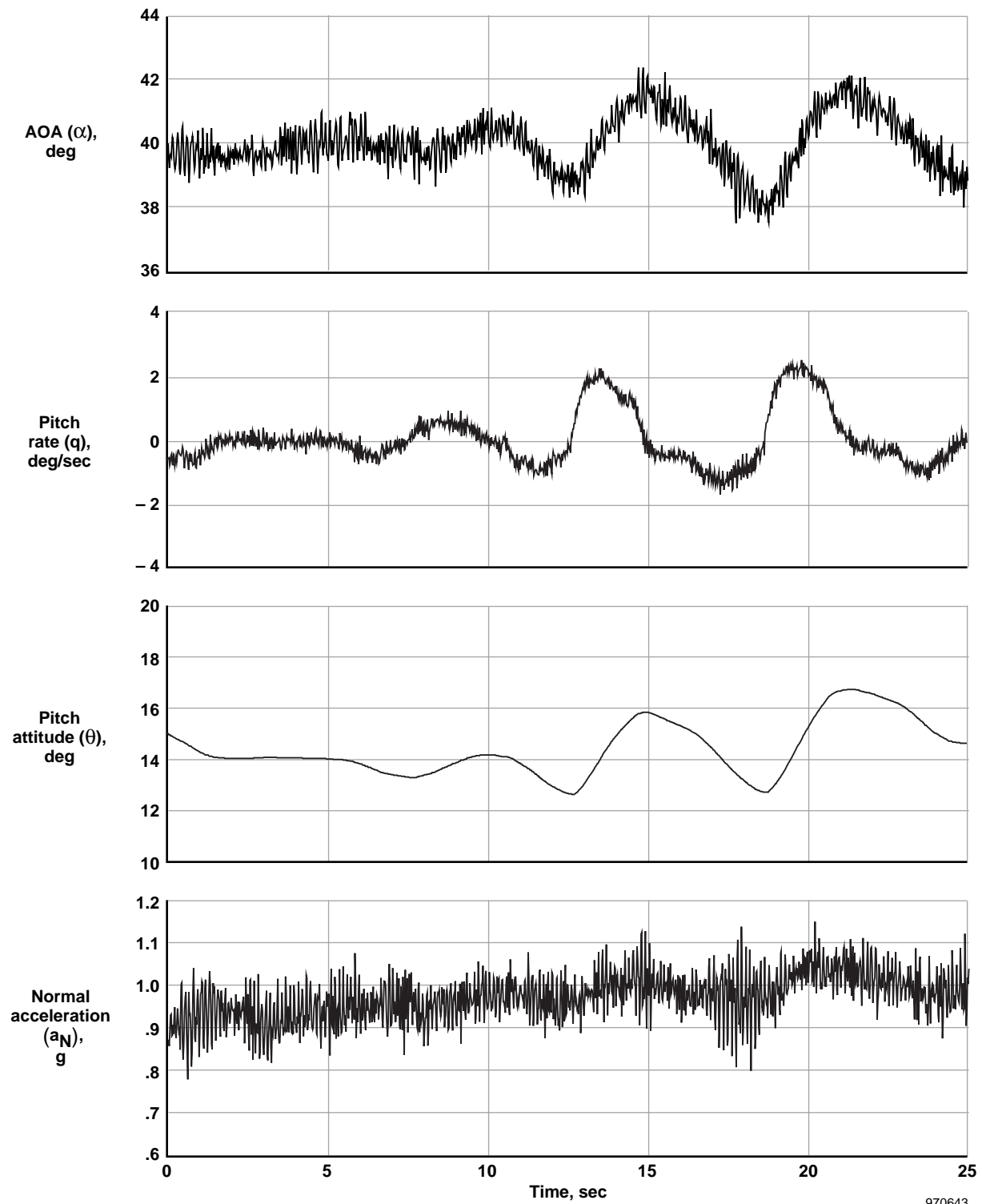
(b) Part 2 of 5.

Figure 10. Continued.
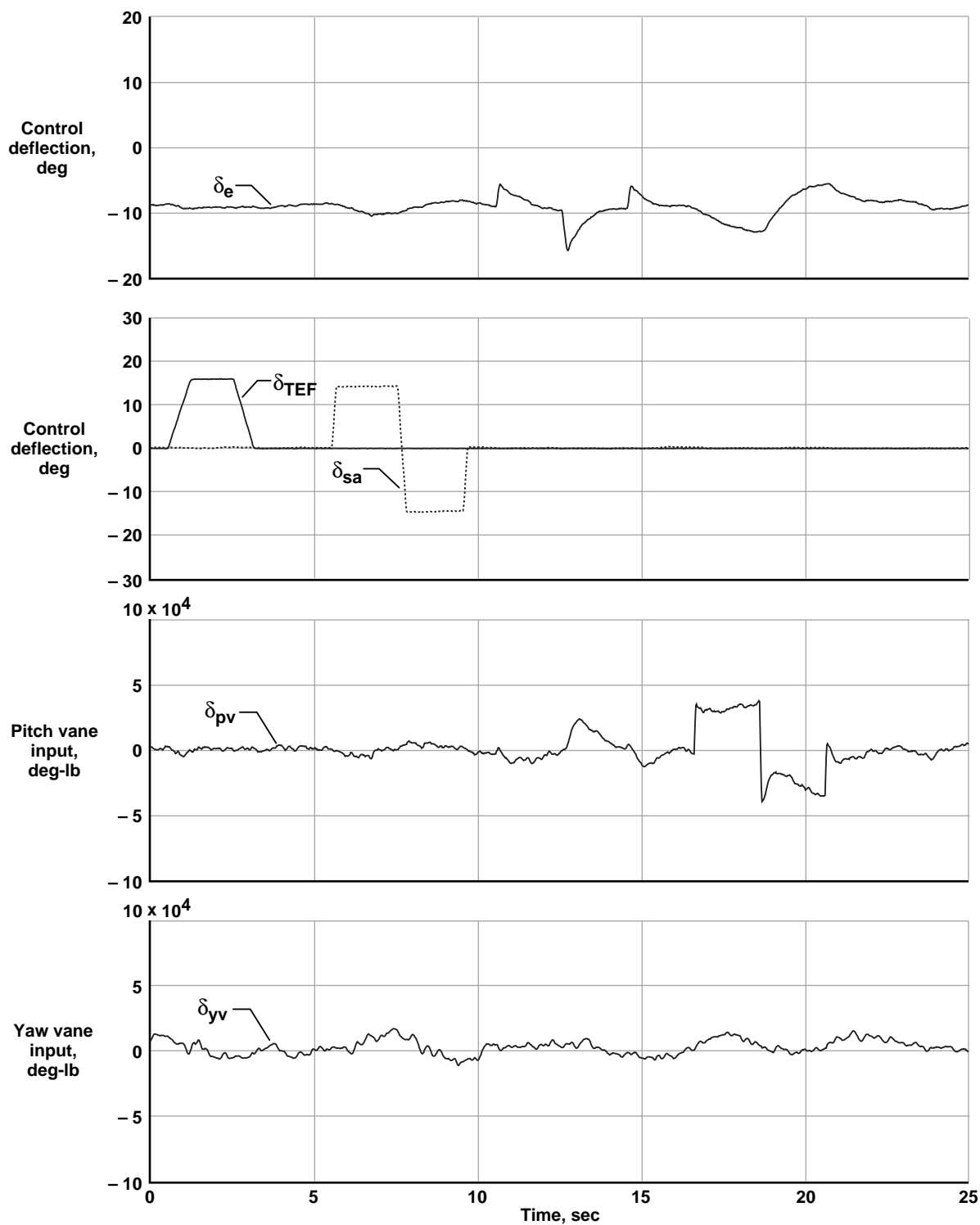
(c) Part 3 of 5.

Figure 10. Continued.

970644
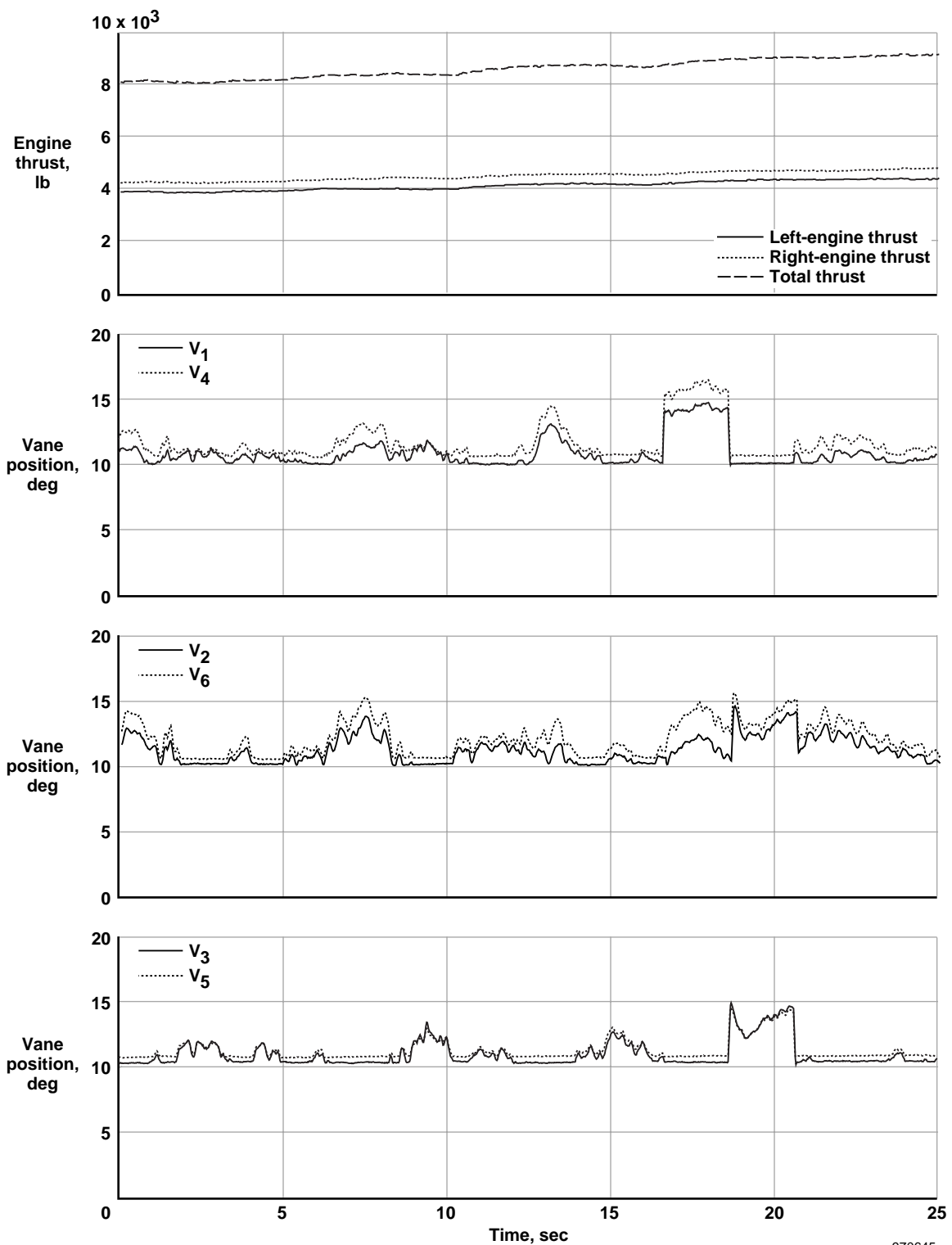
(d) Part 4 of 5.

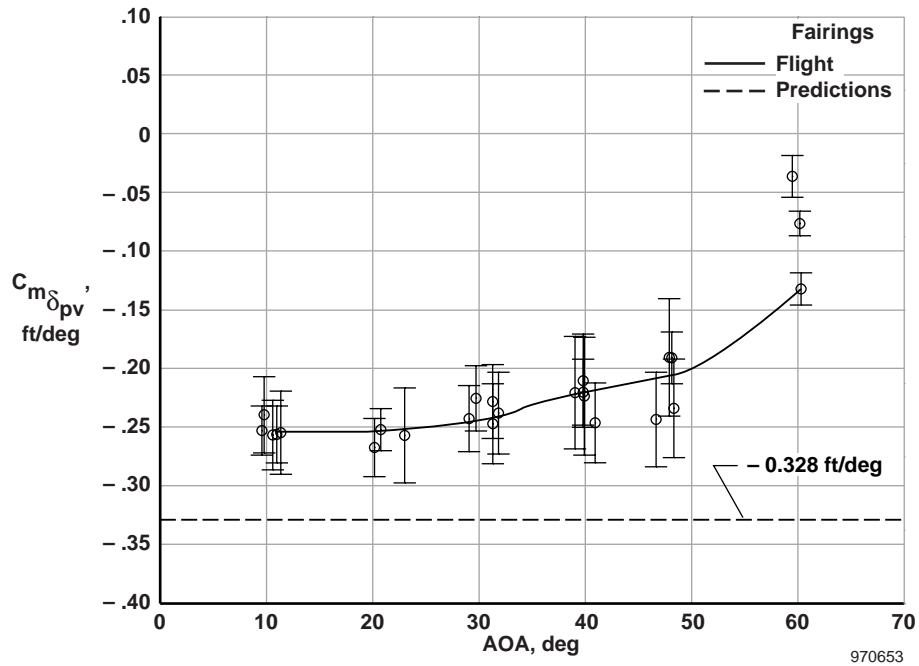Figure 10. Continued.

970645
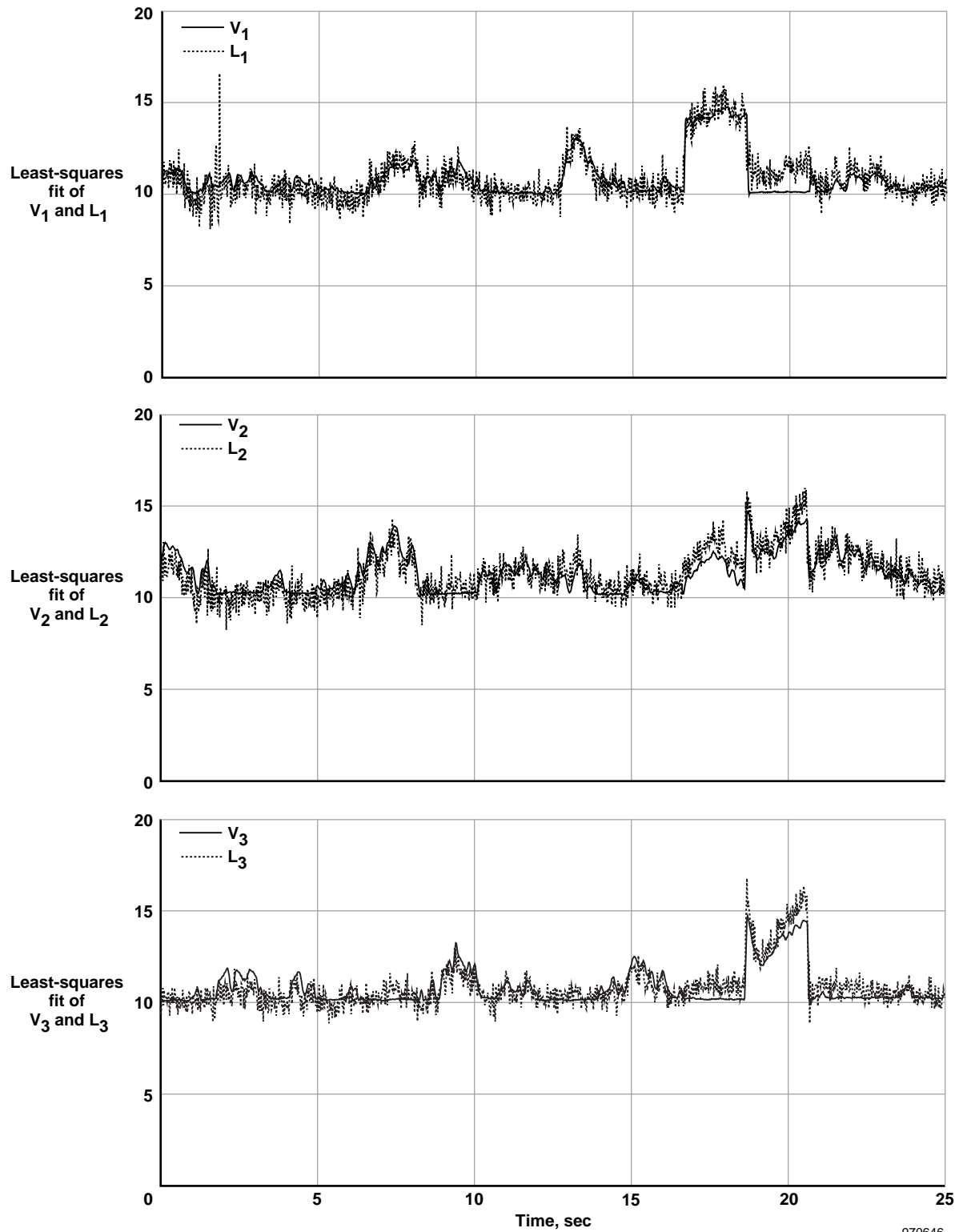
(e) Part 5 of 5.

Figure 10. Concluded.
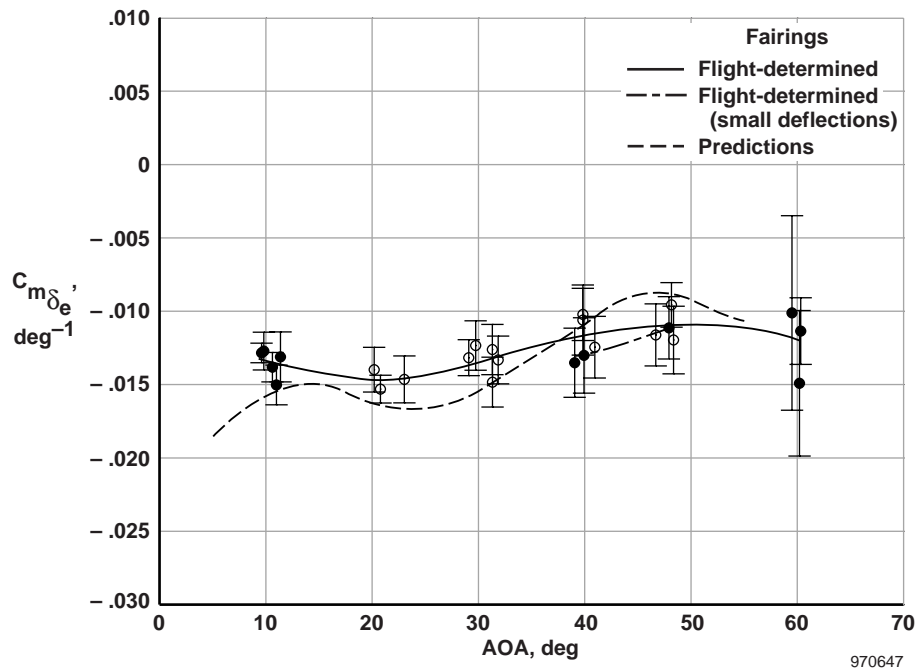
(a) For $C_{m_{\delta_e}}$.
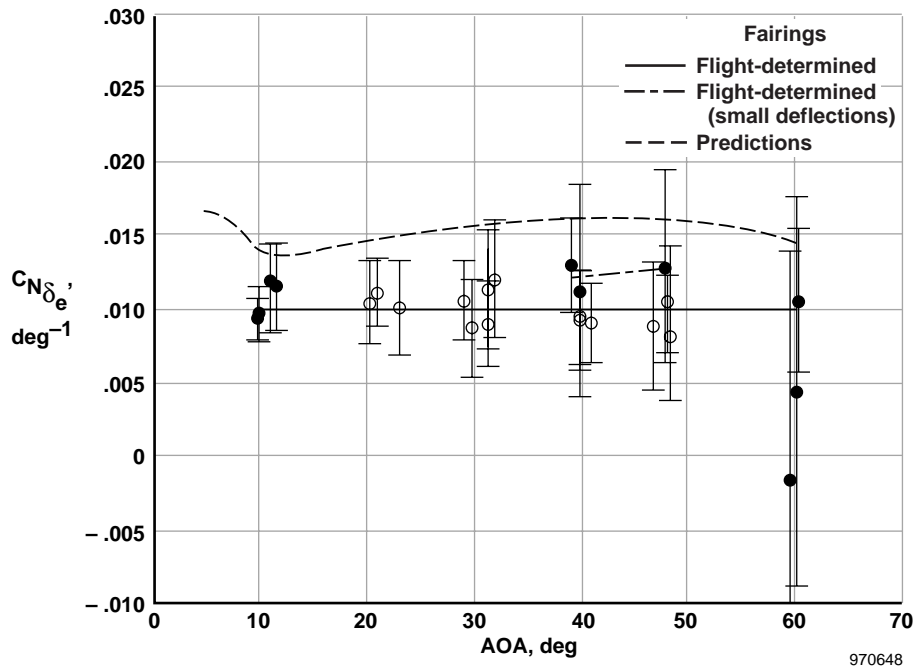
(b) For $C_{N_{\delta_e}}$.

Figure 11. Elevator derivatives as functions of AOA.

60
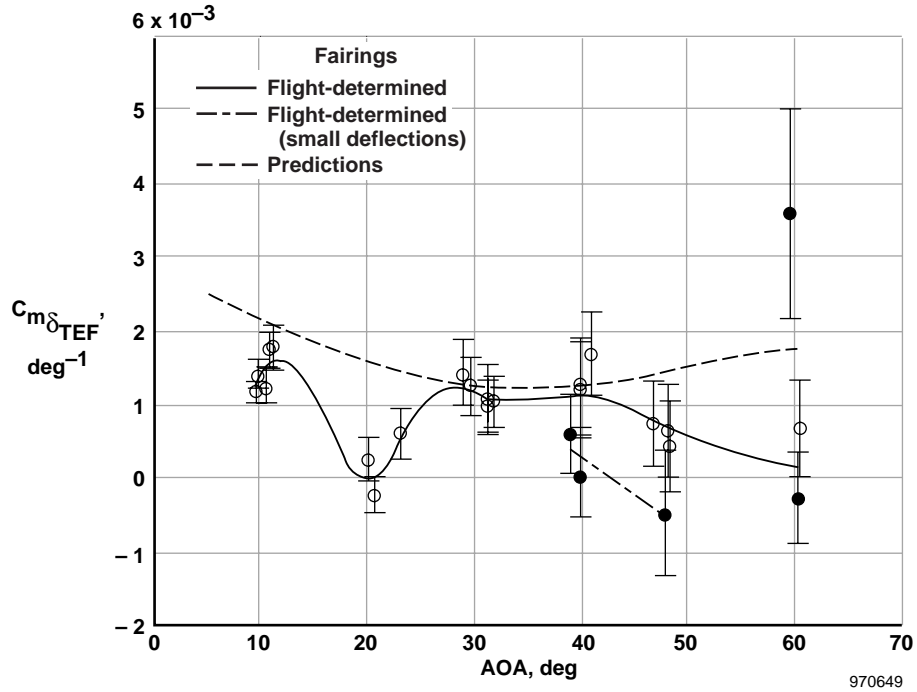
(a) For $C_{m_{\delta_{TEF}}}$.
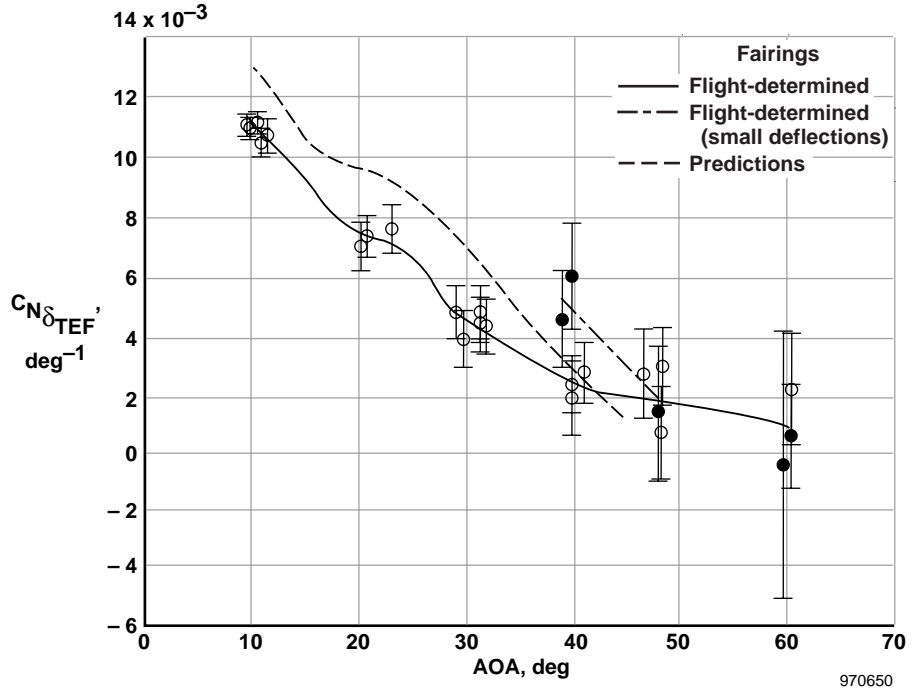
(b) For $C_{N_{\delta_{TEF}}}$.

Figure 12. Trailing-edge flap derivatives as functions of AOA.
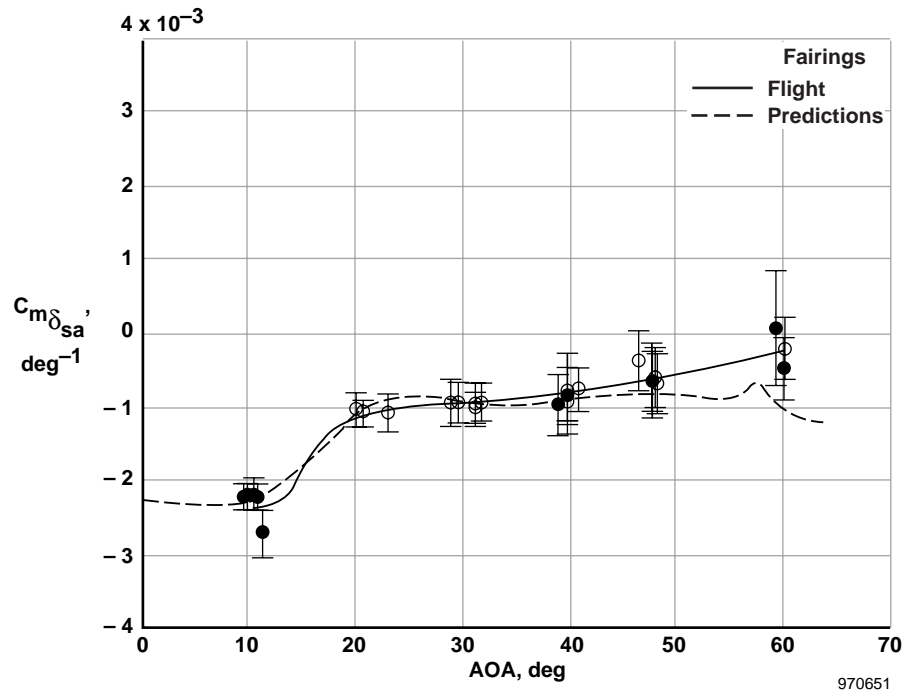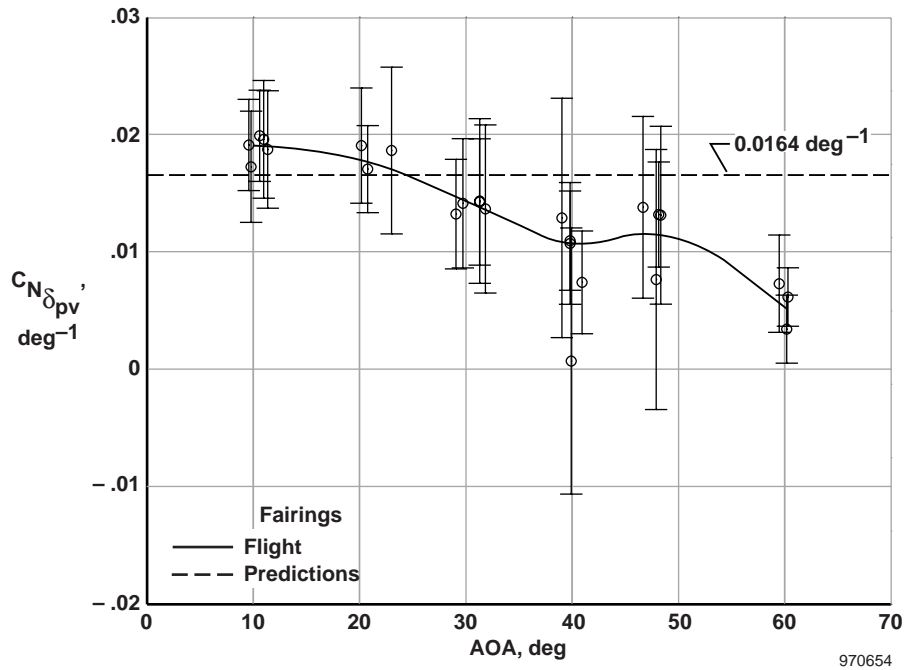
(a) For $C_{m_{\delta_{sa}}}$.
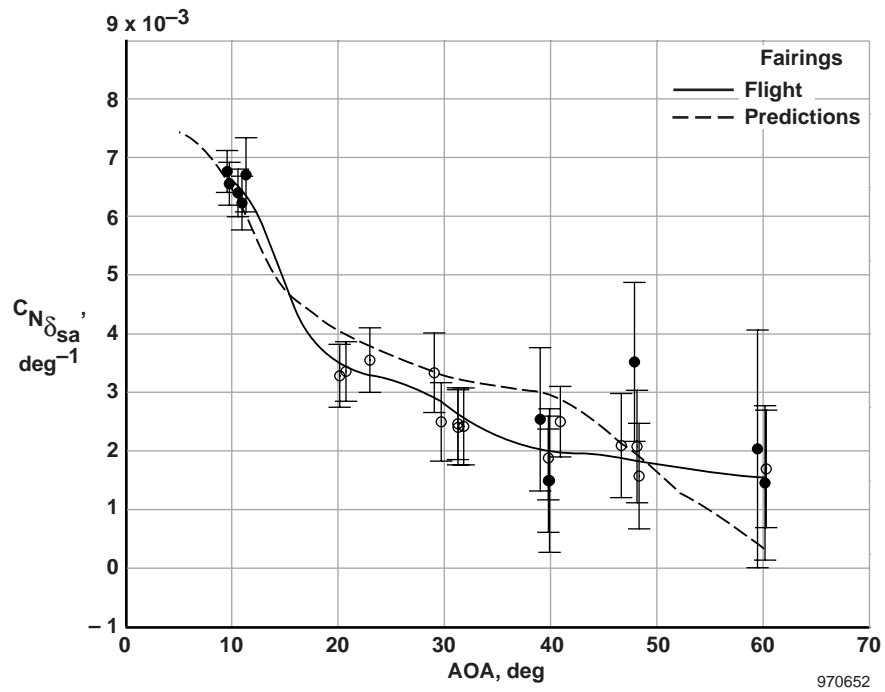
(b) For $C_{N_{\delta_{sa}}}$.

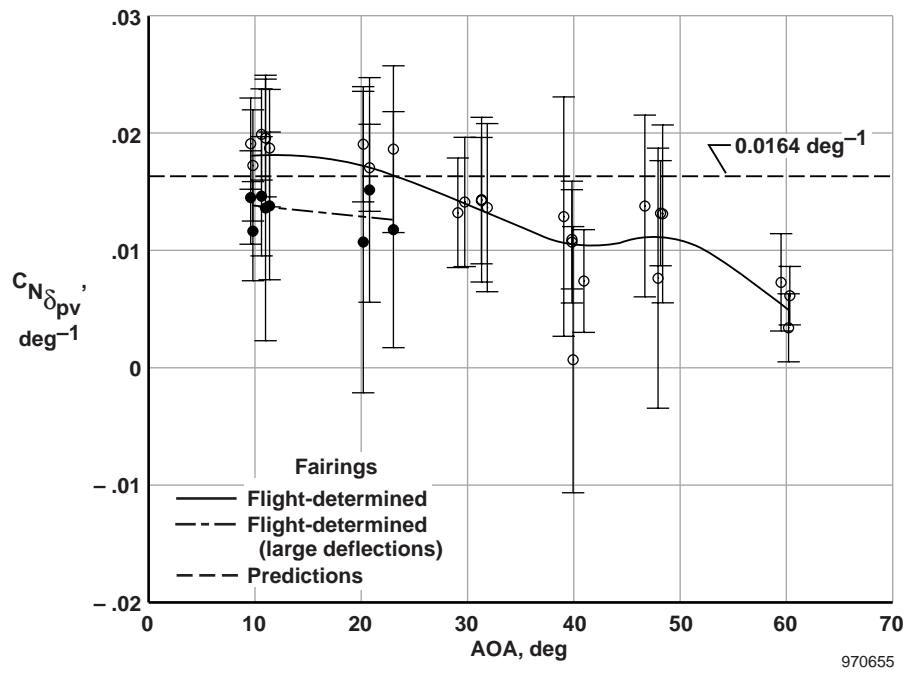Figure 13. Symmetric aileron derivatives as functions of AOA.

(a) For $C_{m_{\delta_{pv}}}$.

(b) For $C_{N_{\delta_{pv}}}$.

Figure 14. Pitch vane thrust-vectoring derivatives as functions of AOA.
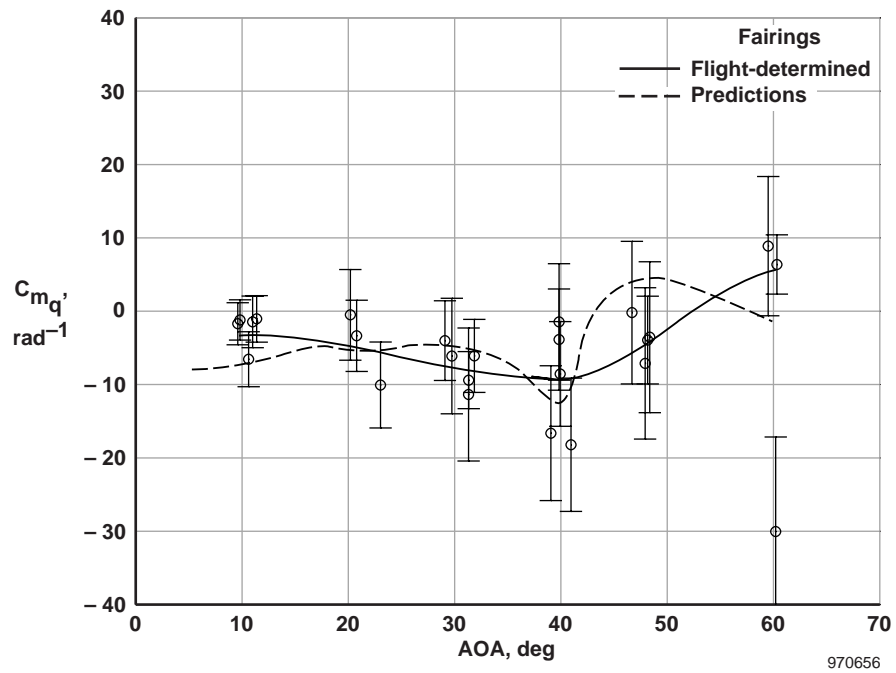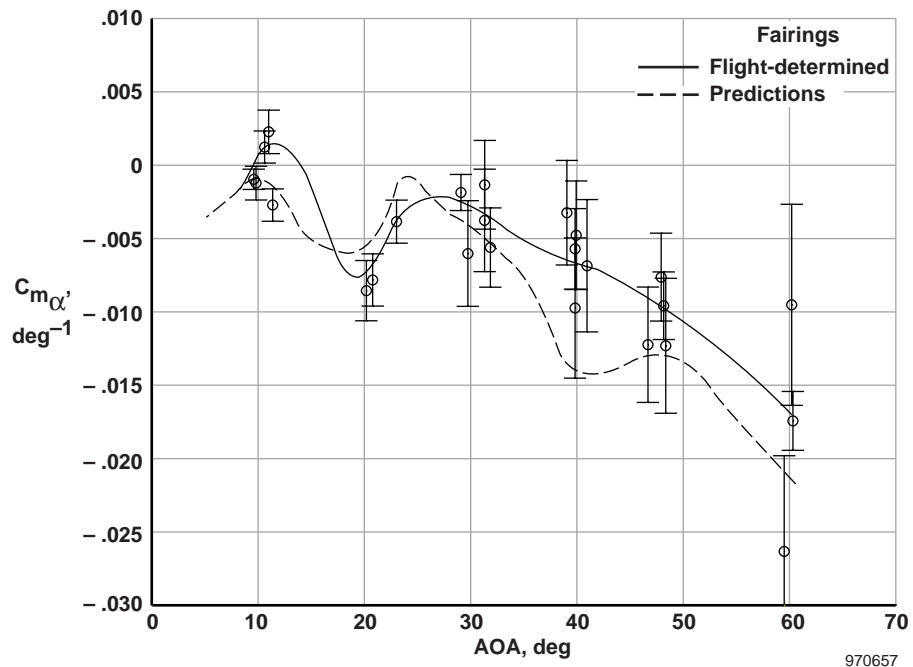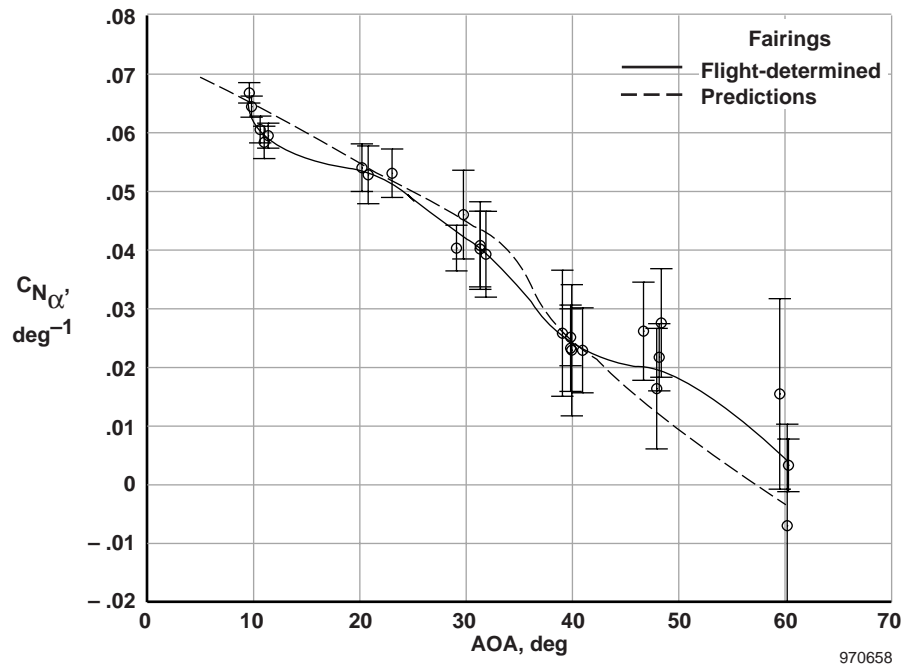
(c) For $C_{N_{\delta_{pv}}}$.

Figure 14. Concluded.

Figure 15. Pitch rate derivative as a function of AOA.

(a) For C_{m_α}.

(b) For C_{N_α}.

Figure 16. Angle-of-attack derivatives as functions of AOA.

REPORT DOCUMENTATION PAGE		Form Approved OMB No. 0704-0188

Public reporting burden for this collection of information is estimated to average 1 hour per response, including the time for reviewing instructions, searching existing data sources, gathering and maintaining the data needed, and completing and reviewing the collection of information. Send comments regarding this burden estimate or any other aspect of this collection of information, including suggestions for reducing this burden, to Washington Headquarters Services, Directorate for Information Operations and Reports, 1215 Jefferson Davis Highway, Suite 1204, Arlington, VA 22202-4302, and to the Office of Management and Budget, Paperwork Reduction Project (0704-0188), Washington, DC 20503.

1. AGENCY USE ONLY (Leave blank)	2. REPORT DATE December 1997	3. REPORT TYPE AND DATES COVERED Technical Paper	
4. TITLE AND SUBTITLE Flight-Determined Subsonic Longitudinal Stability and Control Derivatives of the F-18 High Angle of Attack Research Vehicle (HARV) With Thrust Vectoring			5. FUNDING NUMBERS WU 505 68 50 00 R R 00 000
6. AUTHOR(S) Kenneth W. Iliff and Kon-Sheng Charles Wang			
7. PERFORMING ORGANIZATION NAME(S) AND ADDRESS(ES) NASA Dryden Flight Research Center P.O. Box 273 Edwards, California 93523-0273			8. PERFORMING ORGANIZATION REPORT NUMBER H-2175
9. SPONSORING/MONITORING AGENCY NAME(S) AND ADDRESS(ES) National Aeronautics and Space Administration Washington, DC 20546-0001			10. SPONSORING/MONITORING AGENCY REPORT NUMBER NASA/TP-97-206539
11. SUPPLEMENTARY NOTES			
12a. DISTRIBUTION/AVAILABILITY STATEMENT Unclassified—Unlimited Subject Category 08			12b. DISTRIBUTION CODE

13. ABSTRACT (Maximum 200 words)

The subsonic longitudinal stability and control derivatives of the F-18 High Angle of Attack Research Vehicle (HARV) are extracted from dynamic flight data using a maximum likelihood parameter identification technique. The technique uses the linearized aircraft equations of motion in their continuous/discrete form and accounts for state and measurement noise as well as thrust-vectoring effects. State noise is used to model the uncommanded forcing function caused by unsteady aerodynamics over the aircraft, particularly at high angles of attack. Thrust vectoring was implemented using electrohydraulically-actuated nozzle postexit vanes and a specialized research flight control system. During maneuvers, a control system feature provided independent aerodynamic control surface inputs and independent thrust-vectoring vane inputs, thereby eliminating correlations between the aircraft states and controls. Substantial variations in control excitation and dynamic response were exhibited for maneuvers conducted at different angles of attack. Opposing vane interactions caused most thrust-vectoring inputs to experience some exhaust plume interference and thus reduced effectiveness. The estimated stability and control derivatives are plotted, and a discussion relates them to predicted values and maneuver quality.

14. SUBJECT TERMS Aerodynamics, Flight-to-wind-tunnel comparisons, F-18 Aircraft, High angle of attack, Maximum likelihood estimation, Parameter identification, Stability and control derivatives, Thrust vectoring			15. NUMBER OF PAGES 73
			16. PRICE CODE A04
17. SECURITY CLASSIFICATION OF REPORT Unclassified	18. SECURITY CLASSIFICATION OF THIS PAGE Unclassified	19. SECURITY CLASSIFICATION OF ABSTRACT Unclassified	20. LIMITATION OF ABSTRACT Unlimited